



Annual Review of Vision Science

Measures of Function and
Structure to Determine
Phenotypic Features,
Natural History, and
Treatment Outcomes in
Inherited Retinal Diseases

Artur V. Cideciyan, Arun K. Krishnan,
Alejandro J. Roman, Alexander Sumaroka,
Malgorzata Swider, and Samuel G. Jacobson

Department of Ophthalmology, Scheie Eye Institute, Perelman School of Medicine,
University of Pennsylvania, Philadelphia, Pennsylvania 19104, USA;
email: cideciya@penmedicine.upenn.edu

Annu. Rev. Vis. Sci. 2021. 7:24.1–24.26

The *Annual Review of Vision Science* is online at
vision.annualreviews.org

<https://doi.org/10.1146/annurev-vision-032321-091738>

Copyright © 2021 by Annual Reviews.
All rights reserved

Keywords

autofluorescence, full-field stimulus test, optical coherence tomography,
perimetry, photoreceptors, retina

Abstract

Inherited retinal diseases (IRDs) are at the forefront of innovative gene-specific treatments because of the causation by single genes, the availability of microsurgical access for treatment delivery, and the relative ease of quantitative imaging and vision measurement. However, it is not always easy to choose a priori, from scores of potential measures, an appropriate subset to evaluate efficacy outcomes considering the wide range of disease stages with different phenotypic features. This article reviews measurements of visual function and retinal structure that our group has used over the past three decades to understand the natural history of IRDs. We include measures of light sensitivity, retinal structure, mapping of natural fluorophores, evaluation of pupillary light reflex, and oculomotor control. We provide historical context and examples of applicability. We also review treatment trial outcomes using these measures of function and structure.



1. INTRODUCTION

Inherited retinal diseases (IRDs) make up a heterogeneous group of conditions in which thousands of distinct mutations in more than 300 genes act on rod or cone photoreceptors to cause vision loss that can range from barely noticeable to complete blindness. Some of the genetic causes of IRD are exceedingly rare, whereas others are relatively common (Pontikos et al. 2020, Stone et al. 2017). Across the world, as many as 1 in 3 people may be unaffected carriers, and 1 in 1,000 may be affected by IRDs (Hanany et al. 2020). With the success of gene augmentation therapy in one rare form of IRD (Cideciyan 2010), there has been an explosive interest over the past decade in the development of gene-based or mechanism-specific treatments that aim to improve visual function or slow the progression of IRDs. Dozens of clinical trials have been performed, and scores more are being planned (Garafalo et al. 2020, Scholl et al. 2016, Thompson et al. 2020). In this article, we review some key measures of visual function and retinal structure that may be useful to evaluate phenotypic features and natural history of IRDs and determine efficacy and safety in clinical treatment trials.

2. PSYCHOPHYSICAL MEASURES OF LIGHT SENSITIVITY

Vision is initiated with the absorption of photons in photoreceptors, which in turn activates interneuronal signaling pathways that reach the brain. Psychophysical methods in vision relate physical light stimuli to visual sensations perceived by a subject. Visual acuity is one of the most common psychophysical measures used to determine the extent and progression of visual disability in IRDs and response to interventions. Standard visual acuity measures involve recognition of the smallest high-contrast letters at a distance and provide a measure of spatial resolving power at a single retinal location chosen reflexively by the subject. Retinal locus of gaze during this task is located at either the fovea or another location if the fovea is dysfunctional. Despite its simplicity and widespread acceptance, visual acuity testing does not provide informative insight into visual functioning across the vast expanse of the retina.

Another common psychophysical method is measurement of light sensitivity, which refers to an observer's ability to detect a change in visual stimulation (Hood & Finkelstein 1986). Psychophysical light sensitivity measurements can be performed with focal stimuli, which provide spatial information across the visual field, or with full-field stimuli, which provide no spatial information.

2.1. Light-Adapted Chromatic Perimetry

The focus in studies of IRDs is on photoreceptor disease, and these studies often assume that postreceptoral pathways and higher visual centers are functioning normally. Therefore, a change in light sensitivity can provide a quantitative measure of the main function of photoreceptors. Spatial distribution of light sensitivity corresponding to the spatial distribution of retinal disease severity can be obtained with modern perimeters using computerized methods (Johnson 2013) to stimulate focal regions across the retina and keep track of the patients' responses.

Perimeters can use different colors of stimuli presented on background lights to preferentially test subsets of photoreceptor systems. Most commonly, a white background ($10 \text{ phot}\cdot\text{cd}\cdot\text{m}^{-2}$) is used to desensitize rod photoreceptors, and white stimuli are presented to determine incremental light sensitivities that—in normal subjects—can safely be assumed to be mediated by long-wavelength (LW)- or middle-wavelength (MW)-sensitive cone photoreceptors (LWS/MWS-cones).

In some IRDs, however, LWS/MWS-cone mediation of white-on-white perimetry cannot be assumed; not only short-wavelength (SW)-sensitive cones (SWS-cones) but also light-adapted rods could be mediating or contributing to perception (Tikidji-Hamburyan et al. 2017).



Therefore, our group used monochromatic (600 nm) orange stimuli to minimize stimulation of SWS-cones and rods and maximize stimulation of LWS/MWS-cones (Jacobson et al. 1990, 2010). The most obvious evidence for an unexpected contribution by light-adapted rods to visibility of white-on-white stimuli comes from congenital cone disorders. Subjects with achromatopsia (ACHM) caused by *CNGA3* mutations (Zelinger et al. 2015) demonstrate white sensitivities near or just below the lower limit of normal (**Figure 1a, left**). Sensitivity to orange stimuli presented on the same white background, in contrast, is substantially reduced compared to normal (**Figure 1b, left**). Sensitivity differences between white and orange are consistent with predictions of LWS/MWS-cone mediation in normal eyes but with rod mediation in *CNGA3*-ACHM (**Figure 1c, left**). In blue cone monochromacy (BCM) caused by mutations in LWS/MWS-cone opsin genes (Luo et al. 2015), rods contribute to the visibility of white stimuli but not orange stimuli (**Figure 1a–c, right**). In our group's experience with IRDs, light-adapted chromatic perimetry (LACP) with orange stimuli on a white background provides the most reliable estimates of LWS/MWS-cone function in mild to moderate disease stages of IRDs (Cideciyan et al. 1998, 2020), whereas standard white-on-white stimuli may be better suited to evaluate severe disease stages at the expense of greater uncertainty regarding the source of photoreceptor mediation (Charng et al. 2016, Cideciyan et al. 2018a).

2.2. Dark-Adapted Chromatic Perimetry

Rods not only constitute the great majority of photoreceptors across the retina, but also tend to be among the earliest-affected cells in many IRDs. There are many methods of measuring rod function (McGuigan et al. 2016), and nearly all of them are performed under dark-adapted conditions where both rods and cones could be active. Psychophysical spectral sensitivity functions can clearly distinguish between different photoreceptor types (Cideciyan et al. 1997, 2000, 2013a). However, this approach is more appropriate for a single retinal location and too onerous for the evaluation of regional variation of function sampled across the visual fields of IRD patients. As a substantially more efficient alternative, measurement of sensitivity to two spectrally distinct stimuli has been proposed, in combination with manual (Gunkel 1967, Massof & Finkelstein 1979, Zeavin & Wald 1956) or automated perimetry (Ernst et al. 1983, Jacobson et al. 1986, Roman et al. 2005).

Dark-adapted chromatic perimetry (DACP) in IRD patients provides not only spatial distribution of light sensitivity, but also information regarding rod and cone photoreceptor mediation. A patient with autosomal dominant retinitis pigmentosa (ADRP) due to a Class B *rhodopsin* (*RHO*) mutation followed serially over 30 years with DACP between the ages of 14 and 43 provides an illustrative example (**Figure 2**). Light sensitivity measured with monochromatic 500 nm and 650 nm stimuli (1.7 deg diameter, 200 ms duration) is relatively homogeneous across the retina at age 14. By ages 39 and 43, there is evidence of severe progression across the retina with relative retention of the inferonasal visual field (**Figure 2a**). At a single location in the midperipheral temporal field, progressive changes of rod and cone function can be observed by examining the expected spectral sensitivities from the DACP values (**Figure 2b**). At age 14, the two-color difference is 31 dB, and both colors are rod (R) mediated. Cone sensitivity is not knowable. At age 39, there is a further loss of 22 dB for 500 nm stimulus, but there is a loss of only 14 dB for 650 nm. These results can be explained if the two colors are mixed (M) mediated; that is, the 500-nm stimulus is seen by rods, and the 650-nm stimulus is seen by cones. At age 43, there is yet further loss of 16 dB for 500 nm but no significant change for 650 nm; both colors have become cone (C) mediated, and the rod sensitivity is not knowable. Mediation analyses performed across the visual field demonstrate progression from a nearly complete R-mediated visual field to development of M- and C-mediated locations, except in the case of the inferonasal quadrant.



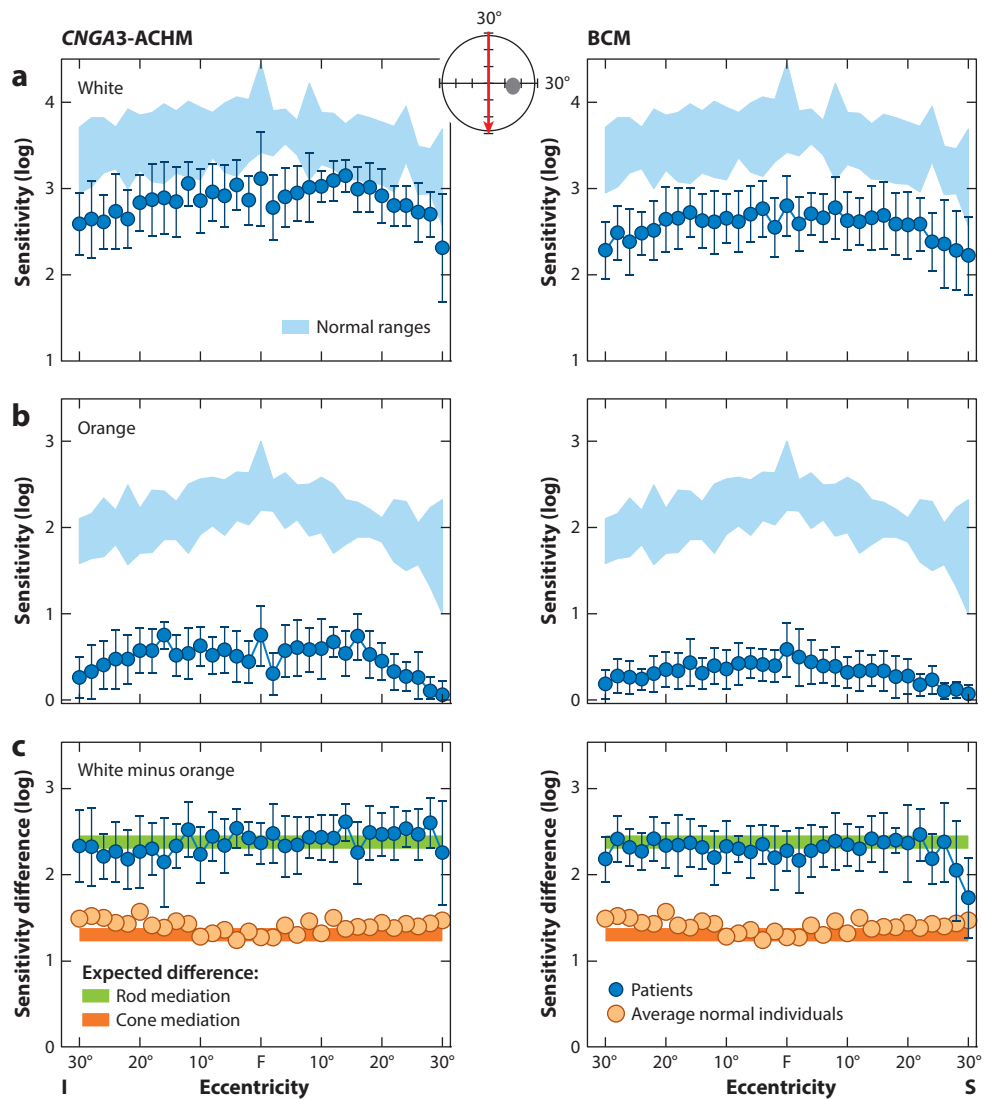
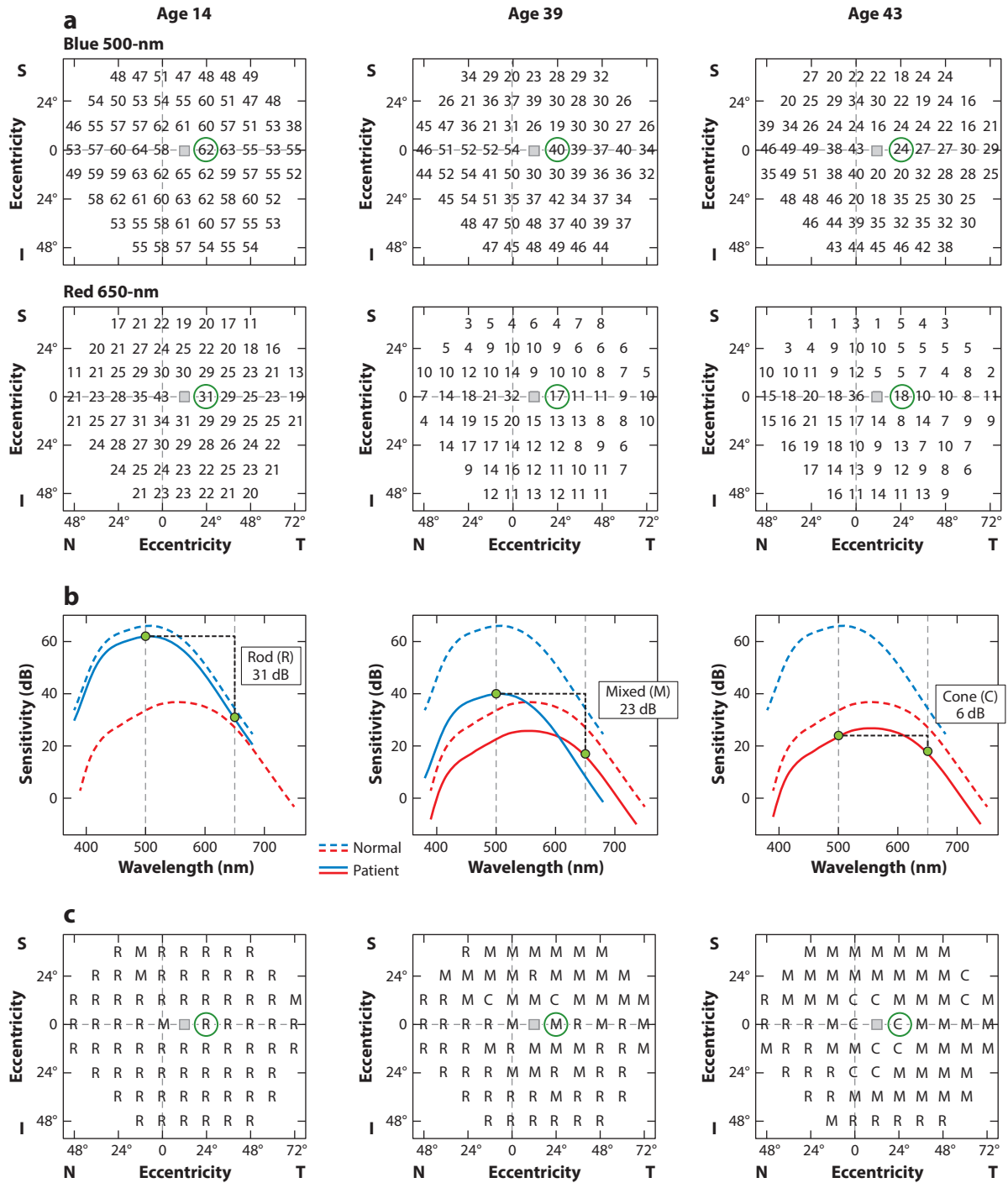


Figure 1

Light-adapted perimetry in congenital cone photoreceptor diseases. (a,b) Sensitivities along the vertical meridian crossing fixation in patients with *CNGB3*-ACHM (left; $n = 9$) and patients with BCM (right; $n = 21$) compared to normal ranges (light blue area; mean ± 2 standard deviation). (a) Broadband white or (b) monochromatic (600 nm) orange stimuli are used on a white background. (c) White minus orange sensitivity difference in patients (blue) compared to average normal individuals (orange). Right column adapted from Luo et al. (2015). Left column adapted with permission from Zelinger et al. (2015), copyright American Academy of Ophthalmology 2015. Abbreviations: BCM, blue cone monochromacy; *CNGB3*-ACHM, *CNGB3*-associated achromatopsia; F, fixation; I, inferior visual field; S, superior visual field.

Our group has used DACP in combination with LACP for more than 30 years to define spatial distribution, progression, and intervention response of rod and cone dysfunction in a wide spectrum of IRDs (Cideciyan et al. 2008, 2009b, 2021; Guziewicz et al. 2018; Haider et al. 2000; Herrera et al. 2008; Jacobson et al. 1995, 2010; Roman et al. 2007; Wright et al. 2004).



(Caption appears on following page)



Figure 2 (Figure appears on preceding page)

Serial DACP measurements performed in a *RHO*-ADRP patient over 30 years. (a) Sensitivity values (in dB) with blue 500-nm and red 650-nm stimuli measured at three ages. Higher values indicate better sensitivity, and lower values indicate worse sensitivity. To equate the two colors for radiance, 16 dB is added to the raw values obtained with the blue stimulus. The green circle represents a single locus further analyzed in panel *b*. Small gray squares demarcate the physiological blind spot. (b) Relative sensitivity values with two stimulus colors at the locus shown in panel *a*. Spectral sensitivity functions associated with rod (*blue solid and dashed lines*) and cone (*red solid and dashed lines*) vision are fit to the DACP values. At age 14, both values are rod (R) mediated, and cone sensitivity is not known. At age 39, the 500-nm stimulus is R mediated, whereas the 650-nm is cone (C) mediated; this is called mixed (M) mediation. At age 43, both stimuli are C mediated. (c) Mediation maps at the three ages across the retina. Spatiotemporal development of R, M, and C mediation with disease progression is shown. Additional abbreviations: DACP, dark-adapted chromatic perimetry; I, inferior visual field; N, nasal visual field; S, superior visual field; T, temporal visual field.

The test–retest variability of DACP has been estimated (Cideciyan et al. 2018a, Roman et al. 2005). To our knowledge, DACP can be performed with at least five types of equipment: the Humphrey field analyzer (Jacobson et al. 1986, McGuigan et al. 2016, Roman et al. 2005), Nidek MP1 scotopic microperimeter (Birch et al. 2011, Crossland et al. 2011, Strauss et al. 2019), MAIA scotopic microperimeter (Pfau et al. 2017), Medmont dark-adapted chromatic LED perimeter (Bennett et al. 2019, Cideciyan et al. 2016), and Metrovision MonCvOne perimeter (Roman et al. 2019, Simunovic et al. 2020). Only two of these choices (Humphrey and Metrovision) can perform both DACP and LACP on the same equipment, allowing estimation of colocalized rod and cone photoreceptor function across the visual field.

2.3. Full-Field Stimulus Test

Early-onset and severe forms of IRDs in the diagnostic category of Leber congenital amaurosis (LCA) cause dysfunction and/or degeneration of outer retinal photoreceptors, either congenitally or in early life. Visual acuities are often severely reduced, and perimetric approaches are not possible, since most subjects with LCA are not able to fixate (Cideciyan & Jacobson 2019; Cideciyan et al. 2009a, 2015a). Our group has previously developed a psychophysical full-field stimulus test (FST) to evaluate visual function in severe vision loss (Roman et al. 2005, 2007) and applied it to improve understanding of the disease stages in different genetic forms of LCA and some IRDs (see Aguirre et al. 2007; Cideciyan et al. 2011; Jacobson et al. 2011a, 2013a, 2017a; Luo et al. 2015).

FST results are dominated by the most sensitive retinal region, which may be located centrally, midperipherally, or in the far periphery (Roman et al. 2005). In LCA patients where reliable perimetry is not possible, the locus of high sensitivity may not be known. Similar to DACP, dark-adapted FST (DA-FST) can be performed with two colors; the difference in light sensitivity between the two colors provides information regarding the dominant photoreceptor type contributing to perception, assuming that both colors are being perceived at the same retinal region. Different background lights can be used in light-adapted FST (LA-FST) to preferentially test subsets of photoreceptor systems. Red and blue stimuli presented on white backgrounds (Cideciyan et al. 2019, 2021; Jacobson et al. 2013a), or red stimuli presented on blue backgrounds and blue stimuli presented on yellow backgrounds (Luo et al. 2015), have been used to probe different cone photoreceptor populations. In all psychophysical methods, the algorithm used for estimation of the threshold can be very important. For FST, our group has used the perimetric standard of 200-ms-long stimuli and a single response button to perform a 4/2 dB staircase to reach two response inversions, having taken the last-seen intensity as the estimated threshold. Several thresholds are quickly repeated per session to obtain intrasession reliability.

Several commercial programs exist that provide testing with some similarity to our group's DA-FST methodology. One of these products is the Diagnosys Full-field Stimulus Threshold (D-FST) program, which provides an estimate of the light sensitivity to variable-length (4 ms or

shorter) stimuli using a proprietary program with forced-choice strategy, auditory cues, and two response buttons to generate a psychometric function (Birch et al. 2020, Klein & Birch 2009). Another commercial program is the Diagnosys FST-dark-adaptation, which uses a single-button response (Cideciyan et al. 2019). Two-color DA-FST was a key outcome measure in our group's gene therapy clinical trial for patients with *RPE65*-associated LCA (Jacobson et al. 2012). White D-FST (Maguire et al. 2009) and two-color Diagnosys FST-dark-adaptation (Cideciyan et al. 2019, 2021) have also been used in clinical trials.

3. STRUCTURAL IMAGING OF THE RETINA AND RETINAL PIGMENT EPITHELIUM

Human retina is an approximately 250- μ m-thick tissue composed of neurons and glia sandwiched between the internal limiting membrane and the retinal pigment epithelium (RPE). The outer retina refers to the distal portion of this tissue, which is composed of approximately 100 million photoreceptor cells organized into an exquisite spatial mosaic. Light-absorbing outer segments of each photoreceptor insert tightly into apical processes of the monolayer of RPE cells, which support phototransduction. Nearly all monogenic defects causing IRDs act upon the outer retina and the RPE. Structural abnormalities caused by IRDs in humans and their animal models have been historically investigated *ex vivo* with light and electron microscopic methods (LaVail 1981, Milam et al. 1998). Three discoveries brought structural measures of the retina and the RPE to living eyes: optical coherence tomography (OCT) (Huang et al. 1991) and two forms of autofluorescence imaging consisting of SW (Delori 1994, Kitagawa et al. 1989, von Rückmann et al. 1995) or near-infrared (NIR) (Cideciyan et al. 2007b, Keilhauer & Delori 2006, Piccolino et al. 1996, Weinberger et al. 2006) excitation lights. We do not cover adaptive-optics imaging in this review, despite its relevance to retinal structure in IRDs (Miller & Kurokawa 2020, Roorda & Duncan 2015).

3.1. Optical Coherence Tomography

OCT uses low-coherence interferometry to measure the intensity of light reflected as a function of depth within the retina. The extreme sensitivity of OCT to small changes in reflection, together with the naturally layered structure of the retina, allows for the differentiation of micron-scale subcellular structures in this nearly transparent tissue.

3.1.1. Interpretation of outer retinal reflections. Initial images of the retina with OCT showed two highly reflective layers that were interpreted as the retinal nerve fiber layer in the inner retina and the RPE and choriocapillaris in the outer retina; specifically, photoreceptor cells were thought to have minimal reflectivity (Hee et al. 1995, 1996; Huang et al. 1991). Our group was the first to recognize that a major reflection originates from near the photoreceptor inner and outer segments; in contrast, the outer nuclear layer (ONL), where the rod and cone nuclei reside, has low reflectivity (Huang et al. 1998, 2000; Jacobson et al. 2000). Our understanding of the correspondence between OCT signals and histologically definable structures has evolved over the past two decades as the axial, lateral, and temporal resolution of OCT systems have improved and as the numbers of observations in molecularly clarified retinal pathology and treatments in humans and animals have increased (Cideciyan & Jacobson 2019; Cideciyan et al. 2011, 2013a, 2020; Drexler et al. 2001; Guziewicz et al. 2018; Hood et al. 2011; Jonnal et al. 2014, 2017; Litts et al. 2018; Liu et al. 2016, 2019; Sajdak et al. 2018; Sakami et al. 2011; Spaide & Curcio 2011; Srinivasan et al. 2008; Zawadzki et al. 2005; Zhang et al. 2021).

Regrettably, the standard nomenclature often used in the retina clinic (Staurenghi et al. 2014) has remained inadequate and confusing. Our current understanding of outer retinal signals in



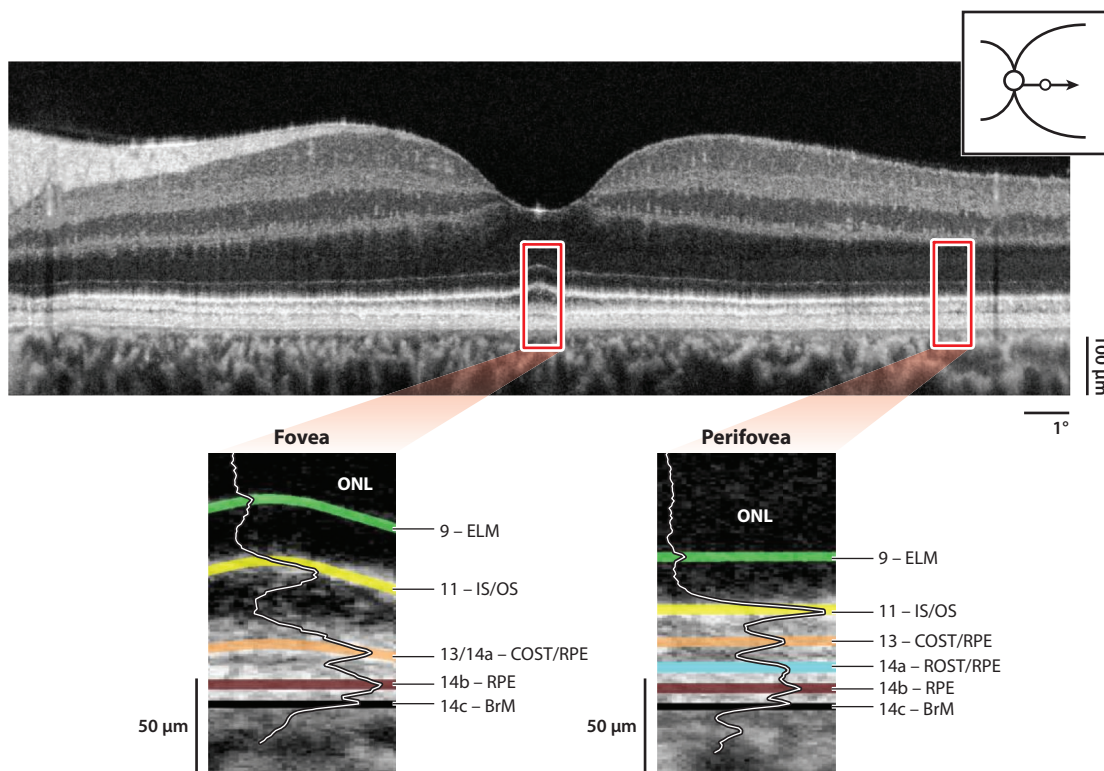


Figure 3

OCT scan along the horizontal meridian through the fovea in a normal subject. The inset shows the location of the scan. Red boxes outline foveal and perifoveal outer retinal regions, which are shown magnified below. Overlaid are the LRP. Hyperscattering signals are highlighted and labeled with the IN.OCT nomenclature or variants thereof. Figure adapted from Cideciyan & Jacobson (2019). Abbreviations: BrM, Bruch’s membrane; COST/RPE, near the interface of cone outer segment tip and RPE contact cylinder; ELM, external limiting membrane; IS/OS, near the junction between inner and outer segments; LRP, longitudinal reflectivity profile; OCT, optical coherence tomography; ROST/RPE, near the interface between rod outer segment tips and RPE apical processes; RPE, near the cell bodies of the retinal pigment epithelium.

a normal human OCT is illustrated in **Figure 3**. In the normal perifovea, there are often six peaks distinguishable on longitudinal reflectivity profiles (LRPs). We label them based on the consensus OCT lexicon (Staurenghi et al. 2014), modifying the labels when necessary. Peak 9 likely originates near the external limiting membrane (ELM), and peak 11 likely originates near the junction of the inner and outer segments (IS/OS). The distance between peaks 9 and 11 is expected to be proportional to the length of inner segments and includes both rods and cones. Peak 13 originates near the tips of cone photoreceptor outer segments and the RPE apical processes that encase them, and the distance between peaks 11 and 13 is expected to be proportional to the length of cone outer segments. The remaining three peaks are labeled peaks 14a, 14b, and 14c because they tend to form a single bright band due to the limited dynamic range of grayscale or pseudocolor clinical OCT images but are often distinguishable into distinct subpeaks when LRPs are considered. Peak 14a likely originates near the tips of rod photoreceptor outer segments and RPE microvilli, and the distance between peaks 11 and 14a is expected to be proportional to the length of rod outer segments. Peak 14b originates in the RPE cell body, and peak 14c originates

near the Bruch's membrane (BrM). Near the center of the fovea, likely corresponding to the rod-free foveola, there is often a small region where peaks 13 and 14a merge and likely represent the tips of elongated cone photoreceptor outer segments and RPE apical processes.

3.1.2. Retinotopic distribution of outer nuclear layer thickness. Monogenetic defects of IRDs are expressed in rod photoreceptors, cone photoreceptors, or RPE cells. Expression is uniform across the retina, but the disease severity often shows large intraretinal variation that remains mostly unexplained. Evaluation of retinotopic disease distribution provides important information regarding the natural history and prognosis, increases our understanding of visual field defects, and can guide localized treatments and assess their consequences. Our earliest studies quantified the topography of the overall retinal thickness to show phenotypic features and intraretinal variation of IRDs (Jacobson et al. 2004, 2005, 2006, 2009c). With better technology and better understanding of outer retinal signals, retina-wide distribution of photoreceptor (ONL) topography was achievable (Cideciyan et al. 2007a, 2008, 2011; Jacobson et al. 2008a,b, 2009c, 2016; Luo et al. 2015).

Current OCT imaging methods do not distinguish between rod and cone photoreceptor nuclei within the ONL. It is well known that, in normal retinas, the foveal ONL consists mostly of cone nuclei, whereas the ONL at the rod ring is dominated by rod nuclei. Very important for the understanding of the evaluation of macular disease are parafoveal regions, where rod and cone densities can be comparable. Our group recently took a first step in attempting to understand rod and cone contributions to the parafoveal ONL by considering patients with normal cone function but lacking rods (Cideciyan et al. 2020).

3.1.3. Progressive changes in outer nuclear layer thickness. The common feature of the natural history of different IRDs involves gradual death of photoreceptor cells and a corresponding progressive thinning of the ONL, but spatiotemporal details of the loss of photoreceptors across the retina and across time can vary dramatically. Based on histopathology of animal models of IRD, it has been hypothesized that photoreceptor loss follows a delayed exponential function, at least to a first approximation (Clarke et al. 2000). Noninvasive OCT imaging allowed for evaluation of this hypothesis in human subjects. To our knowledge, the first estimates of photoreceptor degeneration rate based on serial ONL thickness measurements were made by our group in patients with Usher syndrome due to *MYO7A* mutations (Jacobson et al. 2011b) and in patients with LCA due to *RPE65* mutations who were being evaluated with gene therapy (Cideciyan et al. 2013b). Some scientists doubted that retinal degeneration can be measured in living human eyes [e.g., Wojno et al. (2013) argue that it "...remains difficult to reliably measure change in retinal structure using the ONL metric. ..."]. However, such measurements have become routine in our center for defining the natural history of disease in human patients (Calzetti et al. 2018; Cideciyan et al. 2020; Jacobson et al. 2015, 2017b; Matsui et al. 2016; McGuigan et al. 2017; Sumaroka et al. 2019a) and evaluating interventions in animal models (Beltran et al. 2012, 2015; Cideciyan et al. 2018b; Gardiner et al. 2019).

Importantly, there is sometimes a stage of disease in IRDs where the ONL becomes mildly hyperthick (Jacobson & Cideciyan 2010). This has been detected so far in the foveas of patients with choroideremia (Jacobson et al. 2006), the periphery of patients with *NPHP5*- or *CEP290*-associated LCA (Cideciyan et al. 2011), and immediately surrounding the macular drusen in age-related macular degeneration (AMD) (Sadigh et al. 2013). Mild thickening of the ONL has also been observed in animals as a consequence of interventions or mild disease states (Beltran et al. 2015, Cideciyan et al. 2018b, Guziewicz et al. 2018). It is unlikely that the thickened



ONL observed across diverse IRDs and that observed in AMD arise from the same underlying pathophysiological cause; however, involvement of subclinical edema due to abnormalities at the RPE–photoreceptor interface or reactive gliosis can be postulated at least for some of these cases.

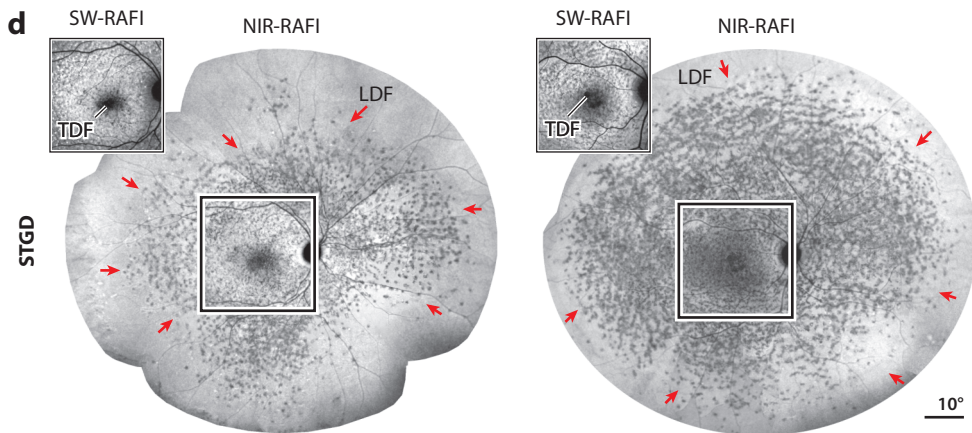
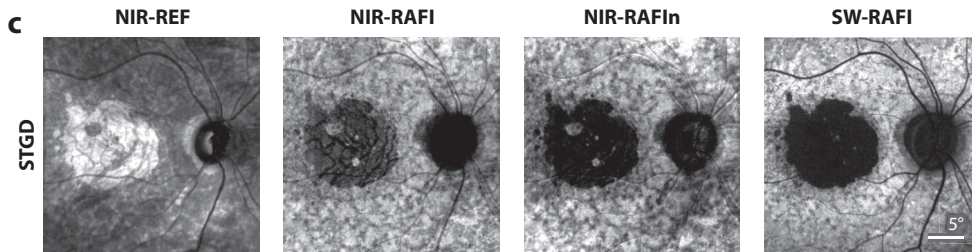
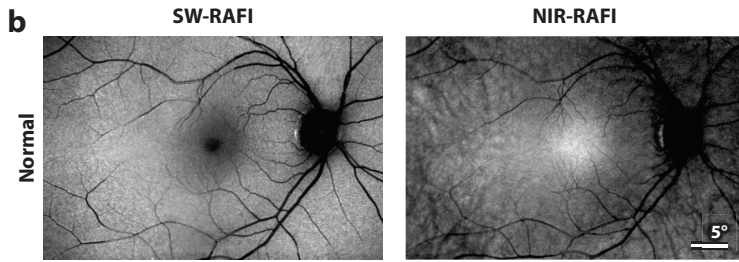
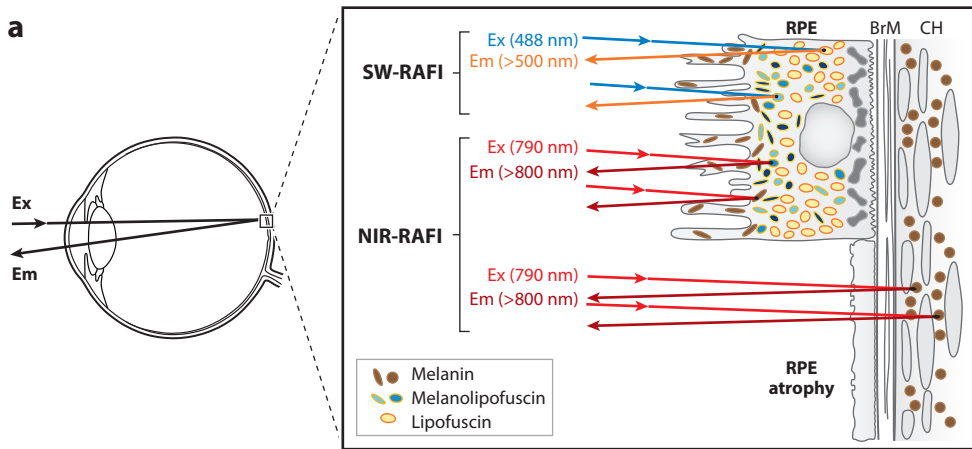
3.2. Autofluorescence Imaging

Distal to the retina are the RPE and choroid layers. RPE cells contain three major pigments: lipofuscin (L), melanin (M), and melanolipofuscin (ML) (Bermond et al. 2020, Feeney 1978, Pollreisz et al. 2020, Weiter et al. 1986). The choroid also contains melanin-related pigments but with physical properties and embryonic origins that are distinct from those of the RPE (Boulton & Dayhaw-Barker 2001, Schraermeyer & Heimann 1999). Lipofuscin-related pigments (L and ML) accumulate with normal aging because of incomplete degradation of material originating from phagocytosis of outer segments. The amounts of melanin-related pigments (ML and M), in contrast, tend to decrease with age (Weiter et al. 1986). All RPE and choroidal pigments have varied but overlapping scattering, absorption, and intrinsic autofluorescence characteristics, and their spatial and axial distribution in health and disease complicate interpretation. This review is limited to two types of autofluorescence signals measurable with noninvasive imaging in living human eyes that likely originate from lipofuscin- and melanin-related pigments (**Figure 4a**).

Conventional autofluorescence imaging of lipofuscin-related pigments of the RPE uses SW and relatively high irradiance excitation lights (Delori et al. 1995, Kitagawa et al. 1989, Sparrow et al. 2020, von Rückmann et al. 1995). Direct evidence in scores of animal studies and circumstantial evidence in human studies have shown that SW lights could confound the natural history of retinal disease in susceptible eyes (Berson 1980; Cideciyan et al. 1998, 2005a; Paskowitz et al. 2006). Thus, it would be prudent to consider the iatrogenic potential of conventional autofluorescence imaging. Our group developed SW-excited reduced-illuminance autofluorescence imaging (SW-RAFI), which substantially reduces retinal irradiance and exposure time (Cideciyan et al. 2007b). SW-RAFI and conventional autofluorescence imaging produce comparable results (Strauss et al. 2016b), and SW-RAFI was used successfully in a multicenter setting for the Progression of Atrophy Secondary to Stargardt Disease (ProgSTAR) studies (Strauss et al. 2016a). A representative SW-RAFI image in a normal eye shows a small dark region at the fovea dominated by absorption of the SW illumination by the macular pigment. An annular region of relatively low intensity surrounds the dark center, and the highest intensities correspond to retinal regions approximately at the eccentricity of the optic nerve head (**Figure 4b**).

NIR excitation results in autofluorescence emissions originating from melanin-related pigments of the RPE and choroid (Cideciyan et al. 2007b, 2015b; Gibbs et al. 2009; Keilhauer & Delori 2006; Piccolino et al. 1996; Taubitz et al. 2019; Weinberger et al. 2006). NIR-excited autofluorescence is inherently low luminance owing to the large separation of this wavelength from the region of peak visual pigment absorption; thus, our group called this modality NIR-RAFI (Cideciyan et al. 2007b). A representative NIR-RAFI image in a normal eye shows a broad region of higher intensity near the fovea (**Figure 4b**).

Several disease processes can result in excessive lipofuscin buildup. In the best-understood example, dysfunction of the photoreceptor disc rim protein ABCA4 results in bisretinoid fluorophores that accumulate as lipofuscin (Sparrow et al. 2012; Weng et al. 1999). Correspondingly SW-RAFI in *ABCA4*-associated retinal degenerations (*ABCA4*-RDs) shows diffuse accumulation of lipofuscin preceding photoreceptor loss and dysfunction (Cideciyan et al. 2004, 2005b, 2007b; Zhang et al. 2015). Unexpectedly, NIR-RAFI also shows homogeneous hyperautofluorescence



(Caption appears on following page)

Figure 4 (Figure appears on preceding page)

Autofluorescence imaging of lipofuscin- and melanin-related pigments. (a) Schematic of retinal autofluorescence emission (Em) signals with short-wavelength (SW; 488 nm) and near-infrared (NIR; 790 nm) excitation (Ex). Dominant interactions are shown for melanin (M), melanolipofuscin (ML), and lipofuscin (L) pigments in cases with intact retinal pigment epithelium (RPE), Bruch's membrane (BrM), and choroid (CH), as well as cases with atrophic RPE. RPE cell drawing based on data from Bermond et al. (2020). (b) SW- and NIR-reduced-illumination autofluorescence imaging (RAFI) in a representative normal individual. Panel adapted with permission from Cideciyan et al. (2007b). (c) Normalization by NIR reflectance (NIR-REF) to reduce the choroidal signal contribution to NIR-RAFI in a patient with Stargardt disease (STGD) with central RPE atrophy. Panel adapted from Cideciyan et al. (2015b). (d) Images from two STGD patients demonstrating major differences in trailing disease front (TDF) at the boundary of central RPE atrophy and in leading disease front (LDF) at the peripheral boundary of local NIR-RAFI heterogeneity. The square indicates the location of the SW-RAFI shown in the inset. Panel adapted from Cideciyan et al. (2015c). Additional abbreviation: NIR-RAFIn, normalized NIR-RAFI.

in *ABCA4*-RD (Cideciyan et al. 2007b). The exact cause of the latter increase is not known, but hypotheses include melanogenesis (Peters et al. 2000, Poliakov et al. 2014) and increased optical cross-section or photo-oxidation of melanin-related pigments. In general, autofluorescence signals with SW and NIR excitation provide complementary and overlapping information.

The natural history of *ABCA4*-RD generally follows a macula-to-periphery expansion of disease sweeping across the retina (Cideciyan et al. 2009b) while avoiding the parapapillary region (Cideciyan et al. 2005b). The movement of the disease front over time can be used as a quantitative measure of disease progression, which is especially important for evaluating the efficacy of interventions. Studies have commonly considered the expansion of RPE atrophy, which is easily detectable as an area lacking autofluorescence signal with SW excitation. NIR-RAFI also shows abnormalities at regions of RPE atrophy, but interpretation of these results is sometimes complicated due to the existence of melanin-based fluorophores within both the RPE and choroid layers. When the RPE is atrophied, the resulting window unmasks the choroidal autofluorescence signal (**Figure 4a**). Our group hypothesized that choroidal melanin has a greater backscatter component than RPE melanin (Cideciyan et al. 2015b) and used normalization by coregistered NIR reflectance (NIR-REF) images to enhance the RPE component and suppress the choroidal component of the NIR-RAFI signal (**Figure 4c**). Quantitative comparison of atrophy areas measured in *ABCA4*-RD patients showed no significant difference between the SW-RAFI and normalized NIR-RAFI approaches. Use of NIR-RAFI for estimating atrophy growth in clinical trials would not only reduce retinal irradiance of actinic lights and make the testing more comfortable, but also allow evaluation of atrophy in retinoid cycle diseases such as *RPE65*-LCA, where natural accumulation of lipofuscin is blocked, and SW autofluorescence is not usable (Cideciyan et al. 2015b).

For many treatment approaches, it is more difficult to stop the degeneration of photoreceptors in retinal areas with severe disease than to prevent the initiation of the earliest stages of disease. RPE atrophy defines the end stage of disease, and the atrophied RPE is often surrounded by regions of severe disease. Thus, measures of atrophy expansion represent the movement of the trailing disease front (TDF), whereas measures of the expansion of the leading disease front (LDF) may be more relevant for most treatments (Cideciyan et al. 2015c). In *ABCA4*-RD eyes, the TDF and LDF can be widely separated where end-stage disease in the macula can be associated with early disease across the retina (**Figure 4d**). The expansion rate of the LDF is often much faster than the growth rate of the atrophy (Cideciyan et al. 2015c). Similar NIR-RAFI methods have been used to define the retained retinal areas in the periphery (Charng et al. 2016), in the macula (Jacobson et al. 2017b), and in paramacular regions (Sumaroka et al. 2019a).

4. FUNCTIONAL IMAGING

In the context of IRDs, functional imaging can be defined as evaluation of multidimensional data that provides insight to the performance of the visual system. Typically, data acquisition is temporally synchronized to a visible stimulus to extract features that are mainly driven by vision. In this section, we review two modalities, pupillometry and oculomotor control, which we find to be particularly promising outcome measures for treatment trials in IRDs. Other functional imaging modalities not reviewed include functional magnetic resonance imaging (fMRI), in which activities in different brain regions stimulated by vision are obtained by detecting changes to local blood flow (Aguirre et al. 2017, Cideciyan et al. 2015a), and functional imaging of the retina involving light-driven changes to reflection or absorption properties or physical movements of reflective boundaries (Bizheva et al. 2006, Guziewicz et al. 2018, Lu et al. 2017, Margrain et al. 2020, Miller & Kurokawa 2020).

4.1. Pupillometry

In the center of the iris is the pupil, through which light passes to reach the retina, thus initiating the earliest stages in vision. The size of the pupil is determined by the relative tone of the sphincter and dilator muscles of the iris and ranges from 1.5 to 8 mm in diameter (Loewenfeld & Lowenstein 1999). Changes to the pupil diameter can be driven by sound, attention, fatigue, memory load, emotion, and other activities within the central nervous system. However, it is the pupillary light reflex (PLR), driven by lights activating retinal photoreceptors (Lowenstein & Loewenfeld 1959), that is most relevant for evaluating vision outcomes.

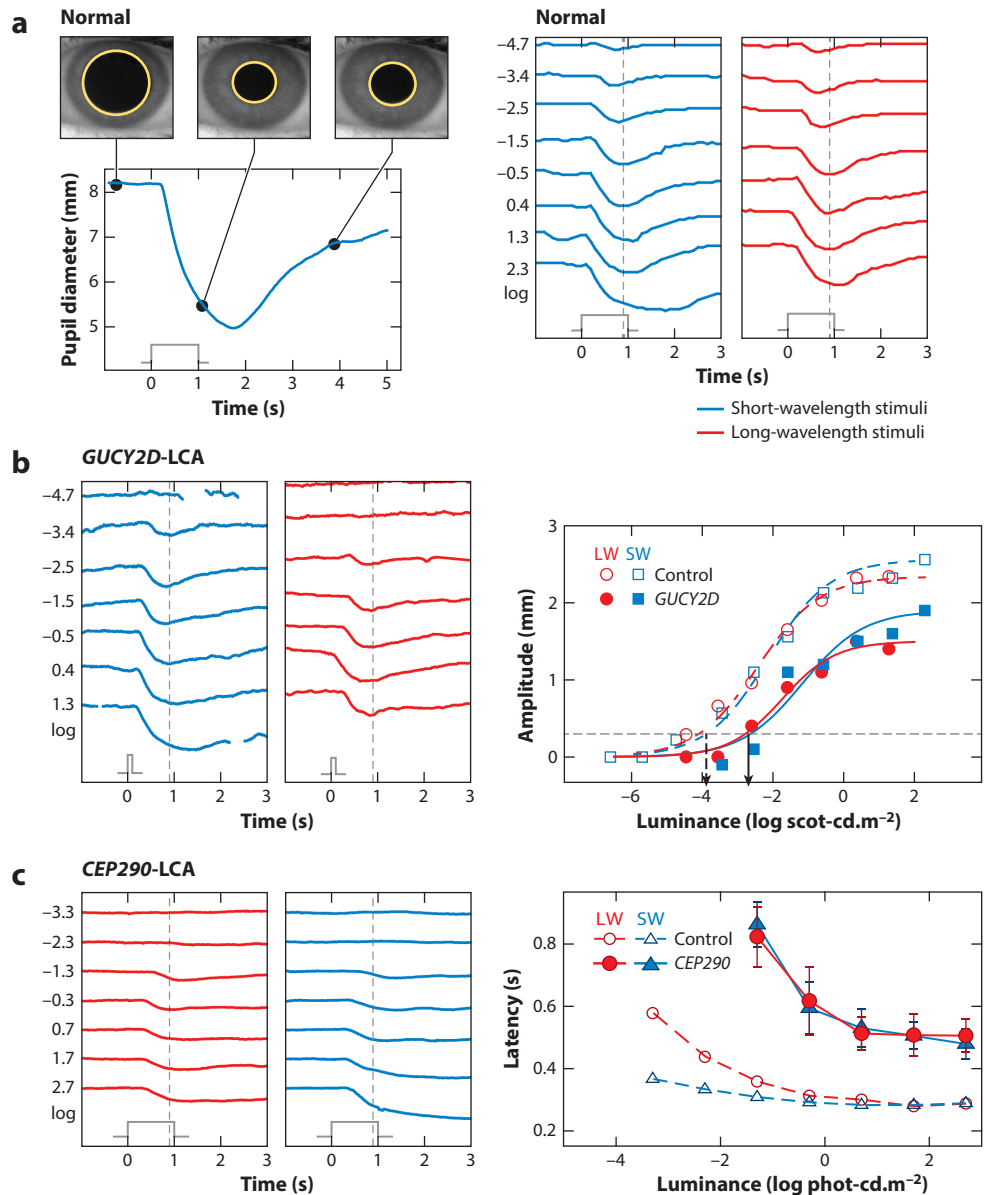
The PLR offers an opportunity to assess the functioning of the visual system by evaluating the combined effects of phototransduction, afferent signal transmission from the retinal photoreceptors to centers in the midbrain, and efferent pathway signaling to the iris muscles. Unlike more common measures of visual function (e.g., visual acuity and perimetry), which are subjective and require the cooperation of the subject, measurement of the PLR is objective and is not affected by the level of cooperation as long as the subject can hold their eyes open for a few seconds. Assuming normal postreceptoral pathways, the PLR can be used to evaluate photoreceptor function objectively in severe forms of human IRDs, as well as in young children who cannot perform psychophysical tasks.

The pupillary pathway includes retinal ganglion cells (RGCs), whose axons form the optic nerve. The optic nerve fibers from the nasal retina of each eye cross at the optic chiasm to the contralateral optic tract, whereas fibers from the temporal retina do not cross but continue as the ipsilateral optic tract. Since both cerebral hemispheres receive information from both eyes, the PLR can be assessed in two ways. The direct PLR measures the pupillary contraction in the eye that was presented with the stimulus, whereas the consensual PLR measures the pupil of the eye that is contralateral to the one presented with the stimulus. Spatial distribution of the light stimulus can be delimited to focal retinal regions, or it can cover the full visual field, taking advantage of the spatial integration properties of the PLR (Schweitzer 1956) and rendering the response independent from the instantaneous direction of gaze. Short-duration stimuli allow the fast and transient PLR (TPLR) to be recorded while minimizing artefacts from blinks and eye movements. This review is limited to our experience with the direct TPLR, with full-field short-duration stimuli presented to dark-adapted eyes.

4.1.1. Quantitative transient pupillary light reflex. The human pupil in primary gaze is normally circular. A TPLR trace consisting of the instantaneous diameter of the dark-adapted pupil plotted as a function of time before and after the onset of a short stimulus can provide



useful quantitative information regarding visual function (**Figure 5a, left**). Major features of the TPLR trace include a steady diameter before the stimulus onset, a rapid constriction phase of the pupil after the stimulus onset, and a redilation phase that slowly returns the pupil size back to baseline. Use of a range of stimuli produces a family of TPLR traces (**Figure 5a, right**), allowing quantitative interrogation of the full dynamic range of the visual system. Complex mathematical models can be used to describe such families. We find that, practically, a small number of easily measured parameters are often adequate to quantitatively define the effects of different photoreceptor diseases and their treatments. One parameter is the baseline pupil diameter, which



(Caption appears on following page)

Figure 5 (Figure appears on preceding page)

Direct transient pupillary light reflexes (TPLRs) in normal subjects and in subjects with retinal disease. (a) A normal TPLR trace (*left*) of pupil diameter change as a function of time after the onset of light (1 s long stimulus monitor shown in gray). Insets show pupil images at three key time points (1 s before and 1 and 4 s after stimulus onset) with margins highlighted for visibility. Families of TPLR traces (*right*) with short-wavelength (SW; *blue*) and long-wavelength (LW; *red*) stimuli over the range of -4.7 to $+2.3$ log scot-cd.m $^{-2}$. Vertical dashed lines mark 0.9 s, which is the point at which the TPLR amplitude is measured. (b) A *GUCY2D*-Leber congenital amaurosis (LCA) patient with rod-mediated TPLRs. The family of TPLR traces (*left*) and luminance-versus-response functions (*right*) with SW (*square*) and LW (*circle*) stimuli are shown. Each family is fit with a hyperbolic function (*dashed curves* for the normal subject and *solid lines* for the patient), and the threshold luminance that evoked a criterion response (0.3 mm, *horizontal dashed line*) is determined. The thresholds are elevated by approximately 1.5 log unit (*x* axis intercepts, *arrowheads*) in the patient compared to the normal subject. Panel adapted from Jacobson et al. (2017a). (c) *CEP290*-LCA patient with cone-mediated TPLRs. The family of TPLR traces (*left*) and latency-versus-luminance functions (*right*) with LW and SW stimuli are shown. Latencies to reach the criterion response of 0.3 mm are considerably slower in patients (*filled symbols*) than in controls (*unfilled symbols*) across the range of luminance. Panel adapted from Krishnan et al. (2020).

provides information about the maximal dilation achieved in the dark-adapted eye. Another parameter is the extent (amplitude) of the pupil constriction achieved early after stimulus onset. We prefer to measure this parameter at a fixed time, rather than the more common approach of measuring the minimum pupil diameter achieved; the timing of the latter approach tends to become progressively delayed with brighter stimuli. Another key parameter is the delay (latency) of the start of pupillary constriction. We prefer to measure the latency as the time to reach a criterion amplitude. Parameters of individual traces are considered across families to estimate the TPLR threshold, which refers to the luminance at which a criterion amplitude is achieved. TPLR thresholds allow for a direct comparison with perceptual or electrophysiologic measures of visual function (Aguirre et al. 2007; Jacobson et al. 2013a, 2017b; Krishnan et al. 2020).

4.1.2. Different photoreceptor systems driving the transient pupillary light reflex. The human TPLR can be driven by the rod or the LWS-, MWS-, and SWS-cone photoreceptors of the outer retina, as well as by the melanopic intrinsically photosensitive RGCs (ipRGCs) of the inner retina (Gamlin et al. 2007, McDougal & Gamlin 2010). Tailored spectral modulations using digital light engines under varied adapting conditions can be used to isolate contributions of individual photoreceptors. However, such specialized testing is usually not practical in a clinical setting with IRD patients, where pupillometry is only one of many tests being performed. Instead, two chromatic stimuli located in the SW and LW regions of the human visible spectrum can be used to identify photoreceptor systems dominating the PLR in an individual. In normal dark-adapted eyes, dim chromatic stimuli that are matched by their scotopic luminance evoke identical PLRs driven by the rod system (**Figure 5b**). With brighter stimuli, responses become more complex, with expected contributions from SWS-cones and ipRGCs to SW stimulation and from LWS/MWS-cones to LW stimulation.

4.1.3. Consequences for transient pupillary light reflex of photoreceptor loss in severe forms of inherited retinal disease. Objective measures of remnant vision in LCA are difficult to obtain. Electroretinograms (ERGs) are often not detectable (Kardon et al. 2011), and fMRI measurements are complicated by severe oculomotor abnormalities. The TPLR, in contrast, is nearly always detectable and can often be interpreted in terms of the function of the remnant photoreceptors.

A subset of patients with various genetic forms of LCA demonstrate profound vision loss with no-light-perception vision. Imaging studies of these patients typically show complete loss of outer retinal structure and relatively retained inner retinal structure (Jacobson & Cideciyan 2010, Jacobson et al. 2013b). Charng et al. (2017) quantified the direct TPLR in such patients, in whom signaling from all rod and cone photoreceptors across the retina is expected to be lacking. With typical stimuli, TPLRs were not detectable. With longer-duration or brighter short-duration stimuli, robust TPLRs were detectable in the majority of patients with profound vision loss. These TPLRs had small amplitudes and substantially delayed latencies and likely represented the activation of human ipRGCs in isolation from rod or cone photoreceptor input (Charng et al. 2017).

Many LCA patients have some remnant vision originating from partially functioning rod or cone photoreceptors, and our group has spent two decades evaluating them with the objective functional imaging approach afforded by the direct TPLR (Aguirre et al. 2007; Aleman et al. 2004; Charng et al. 2017; Jacobson et al. 2009b, 2011a, 2013a, 2017a,b; Krishnan et al. 2020). The abnormal pupillary reactions that have been qualitatively observed had long been considered to be a feature of the clinical presentation of patients with LCA. Our group developed methods to record TPLRs using a range of stimuli extending over approximately 9 log units to quantify visual function in dark-adapted eyes (Aleman et al. 2004). Our group showed that sluggish responses in LCA can mostly be explained with loss of quantum catch at the outer retinal photoreceptors, and TPLR latencies can be normal when adjusted for individual differences in sensitivity resulting from the biochemical block of chromophore supply to both rods and cones in *RPE65*-associated LCA (Aguirre et al. 2007). In other studies, our group used chromatic TPLRs to provide objective evidence for unexpectedly retained rod function in *AIPL1*-associated LCA (Jacobson et al. 2011a) and an unexpectedly large spectrum of rod dysfunction in *GUCY2D*-associated LCA ranging from near normal (**Figure 5b**) to complete loss (Jacobson et al. 2013a). In a larger cohort of *GUCY2D*-LCA, chromatic TPLR results could differentiate between individuals with remnant cone function and those with remnant rod function (Jacobson et al. 2017a). In another molecular form of LCA due to *CEP290* mutations, our group found TPLRs with slow latencies (**Figure 5c**) dominated by remnant foveal cones (Jacobson et al. 2017b). More recently, our group provided a hypothesis to explain how individual differences in parafoveal remnant vision contribute to differences in TPLR latency in *CEP290*- and *NPHP5*-associated LCA (Krishnan et al. 2020).

4.1.4. Transient pupillary light reflex–based outcome measures in clinical trials. The TPLR has been and continues to be used as an objective outcome measure in clinical trials evaluating interventions in severe forms of IRDs (Thompson et al. 2020). Our group's *RPE65* gene augmentation therapy measured chromatic TPLR amplitudes at fixed times across a range of luminances and derived the threshold to reach a criterion amplitude as the objective outcome measure (Cideciyan et al. 2008, Jacobson et al. 2012). At baseline, the TPLR of *RPE65*-LCA eyes were 5.6 log units less sensitive than normal eyes, similar to the 5.5-log-unit loss of sensitivity measured with subjective perception. After treatment, there were highly significant changes, with a 1.2-log-unit improvement of TPLR thresholds on average (Cideciyan et al. 2008, Jacobson et al. 2012). More recently, in a clinical trial evaluating the efficacy of an antisense oligonucleotide, our group showed correspondence between objective visual function improvements with TPLR and subjective vision improvements (Cideciyan et al. 2021). Test–retest variability of TPLR parameters has been quantified, and TPLR protocols are being used as objective outcomes in several ongoing clinical trials (Jacobson et al. 2017a,b; Krishnan et al. 2020; Lisowska et al. 2017). The TPLR can also be used as an inclusion criterion to confirm functional fidelity of the

retinopretectal tract, despite lack of light perception in patients who would be candidates for retinal regenerative therapies such as those involving optogenetics (Jacobson & Cideciyan 2010).

4.2. Oculomotor Control

Perception of fine visual detail in normal eyes requires a complex oculomotor system that maintains correspondence between a feature of interest and the fovea (Kowler 2011). In IRDs with congenital vision loss, the visual feedback necessary for normal development of the oculomotor system is interrupted. In later-onset IRDs, foveal disease causes abnormalities in the oculomotor system. Depending on the timing and severity of the vision loss, a wide spectrum of oculomotor abnormalities can occur, ranging from classic sensory defect nystagmus (instability of fixation but retained ability to find and attend to a visual target) to wandering eyes (complete lack of oculomotor control). Our group has developed two functional imaging modalities to quantify the range of oculomotor abnormalities observed in different IRDs.

Nystagmus recordings primarily aim to measure the instantaneous gaze to a target over time with respect to the location of the fovea. It is generally assumed that the target is visible to the subject. In patients with IRDs, differences in visual sensitivity and/or visual field may limit visibility of the target such that what is visible to some patients is not visible to others. In *RPE65-LCA*, for example, major differences in rod and cone sensitivities make it difficult to know a priori what target luminances may be comparably visible across a cohort of patients (Aguirre et al. 2007; Jacobson et al. 2007, 2009a). Accordingly, our group developed a method to measure nystagmus as a function of target luminance in IRDs by explicitly including the following three key aspects. First, NIR illumination was used to record the instantaneous location of the target with respect to the anatomical fovea at video rate. Second, all testing was performed in darkness such that there were no visible distractions beyond the target. Third, recording epochs always started with a high-luminance target easily visible to the subject, and lower-luminance targets were then tested to obtain nystagmus parameters as a function of the luminance straddling visibility threshold of each individual.

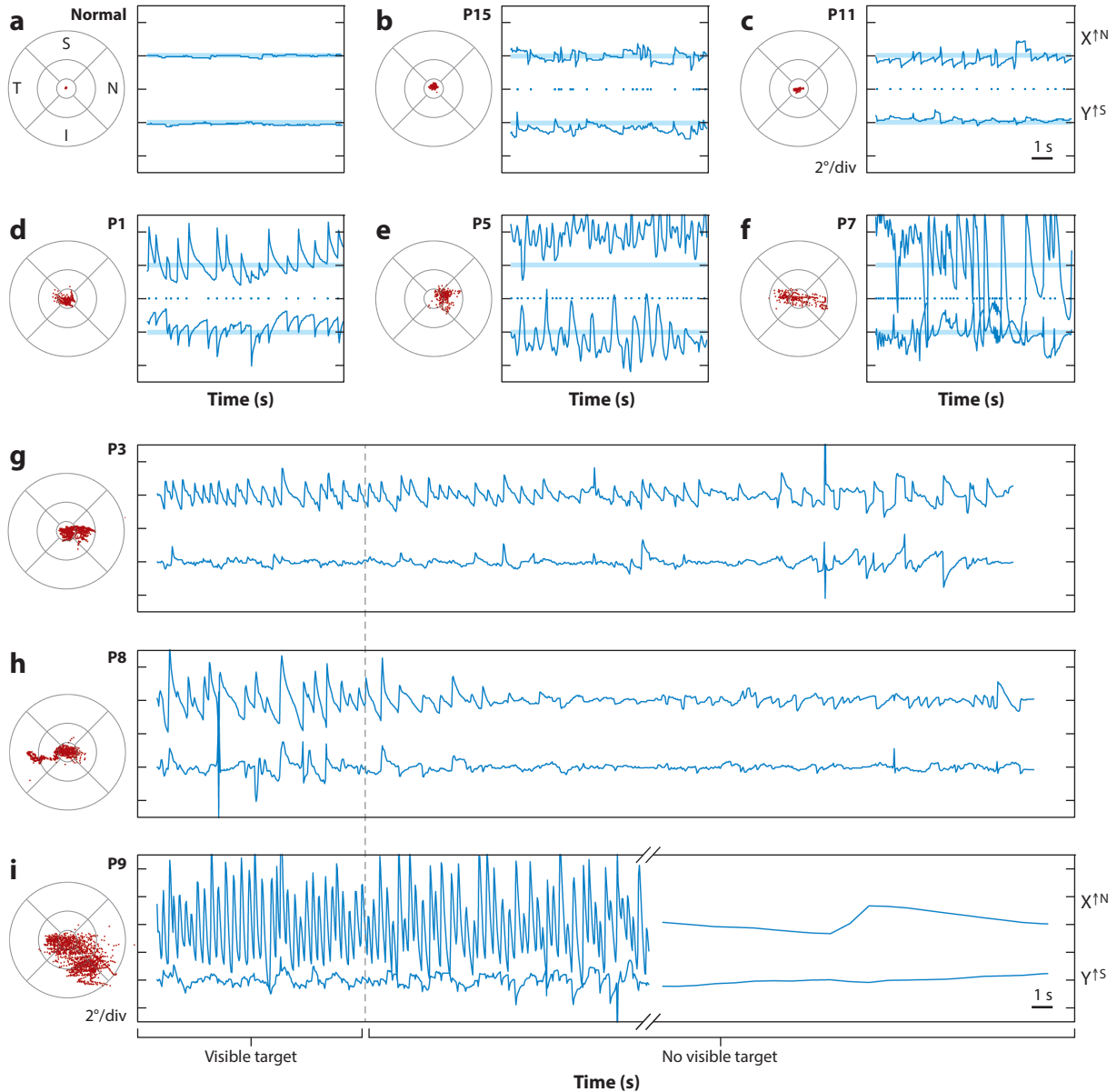
The five *RPE65-LCA* eyes shown in **Figure 6** demonstrate the spectrum of oculomotor abnormalities observed. P15, P11, and P1 are patients with minor (**Figure 6b,c**) or moderate (**Figure 6d**) oculomotor abnormalities, although they retain foveal fixation. P5 and P7, in contrast, demonstrate more severe stages of disease with extrafoveal fixation (**Figure 6e**) or very large-amplitude nystagmus (**Figure 6f**). To understand the extent of the visual feedback on nystagmus, our group performed recordings of long duration that included an initial period in which a stimulus perceptible to the eye was tested, followed by a longer period without the stimulus. Three examples demonstrate the range of observations upon removal of the visible target. In P3, there is very little change in the amplitude of the nystagmus as the fixation location slowly drifts nasally away from the fovea, and there is a slight reduction in the frequency of nystagmus (**Figure 6g**). In P8, there is substantial dampening of the nystagmus amplitude and frequency, along with drift of the retina away from where the visible target was earlier (**Figure 6h**). In P9, there is initially no change in the amplitude or frequency of the nystagmus for nearly 30 s as the fixation location drifts away from the fovea. Afterward, however, the jerk component of the nystagmus completely disappears, and there remains only a slow drift (**Figure 6i**).

Quantitation of oculomotor characteristics can help interpret the consequences of treatments attempting to improve vision. Our group provided evidence for emergence of new or additional fixation locations in a subset of patients following gene therapy but found no evidence of a decrease in amplitude or frequency of nystagmus (Cideciyan et al. 2008, 2009a, 2015a).

At the most severe end of the LCA spectrum are patients who report being congenitally blind and having never experienced visual perception. Lack of visual experience in early childhood leads



to the failure to develop any oculomotor control and wandering eyes (Kömpf & Piper 1987, Leigh & Zee 1980). Since reproducible retinal imaging over any length of time is often not possible in severe LCA, our group developed a simple corneal video imaging method to record oculomotor control and instability in any retina clinic (Jacobson et al. 2017b). Quantitative analyses of videos recorded in the dark with and without a fixation target allow better understanding of visual feedback to the oculomotor system in patients with very severe vision loss. The method has been used as an outcome measure in a clinical trial where early results suggest efficacy (Cideciyan et al. 2019, 2021).



(Caption appears on following page)

Figure 6 (Figure appears on preceding page)

Range of nystagmus features in *RPE65*-LCA. (a–f) Results from (a) a representative normal subject are compared to patients (b) P15, (c) P11, (d) P1, (e) P5, and (f) P7. For each subject, 10-s-long epochs of eye movement data during fixation to a large visible target are shown in spatial and spatiotemporal coordinates. Spatial distribution of fixation clouds are shown on standard circles (with radii at 1.65°, 5°, and 10°) representing the macular region centered on the anatomical foveal depression. Spatiotemporal distribution of eye movements are shown on chart records for X and Y directions; up is N for X and S for Y. All results are presented as equivalent right eyes for comparability. Horizontal lines (light blue) on the chart records depict the location of the anatomical fovea. Dots between X and Y traces represent the timing of the high-frequency eye movements. (g–i) Representative fixation records from (g) P3, (h) P8, and (i) P9 demonstrating the interindividual differences in nystagmus waveforms as a function of the visibility of the target in an otherwise darkened ambient environment. Low-frequency components have been removed from the long-duration X,Y chart records (but not from the fixation clouds shown on standard circles) to better demonstrate nystagmus characteristics as the eyes drift away from the anatomical fovea upon extinguishing of the visible target. The break in axis for P9 represents the period of 25 to 80 s. Figure adapted from Cideciyan et al. (2015a). Abbreviations: div, division; I, inferior retina; LCA, Leber congenital amaurosis; N, nasal retina; S, superior retina; T, temporal retina.

5. CONCLUSIONS

An important prerequisite for the successful development of new therapies for IRDs is better understanding of the visual dysfunction, structural abnormalities, and natural progression associated with these genetically and clinically heterogeneous conditions. The ease of optical access to the retina for imaging, combined with the exquisite dynamic range of human vision, provides scores of possibilities for measurement. In this article, we review a small subset of measurements that we have found useful and informative in IRDs. Of course, all measures will not be appropriate for all patients. Selections will have to depend on many factors, such as the primary disease pathology, stage of severity, and level of cooperation expected. In terms of patients retaining stable fixation, for example, perimetric methods of LACP and DACP provide excellent information content regarding the spatial distribution of function across different photoreceptor types, whereas FST methods are more appropriate for patients without stable fixation. Objective measures of visual function, such as pupillometry, can complement perceptual measures such as perimetry. Micron-level features can be easily measured and interpreted in terms of subcellular photoreceptor features. Better understanding of vision deficits in IRDs will require building quantitative models relating visual function and retinal structure. Our group has performed some of the initial studies in this endeavor (Cideciyan et al. 2008, 2020; Jacobson et al. 2005; Sumaroka et al. 2019b), but modeling more complex structure–function relationships remains an important challenge to the field.

DISCLOSURE STATEMENT

The authors are not aware of any affiliations, memberships, funding, or financial holdings that might be perceived as affecting the objectivity of this review.

LITERATURE CITED

- Aguirre GK, Butt OH, Datta R, Roman AJ, Sumaroka A, et al. 2017. Postretinal structure and function in severe congenital photoreceptor blindness caused by mutations in the *GUCY2D* gene. *Investig. Ophthalmol. Vis. Sci.* 58(2):959–73
- Aguirre GK, Komáromy AM, Cideciyan AV, Brainard DH, Aleman TS, et al. 2007. Canine and human visual cortex intact and responsive despite early retinal blindness from *RPE65* mutation. *PLOS Med.* 4(6):1117–28
- Aleman TS, Jacobson SG, Chico JD, Scott ML, Cheung AY, et al. 2004. Impairment of the transient pupillary light reflex in *Rpe65*^{-/-} mice and humans with Leber congenital amaurosis. *Investig. Ophthalmol. Vis. Sci.* 45(4):1259–71



- Beltran WA, Cideciyan AV, Iwabe S, Swider M, Kosyk MS, et al. 2015. Successful arrest of photoreceptor and vision loss expands the therapeutic window of retinal gene therapy to later stages of disease. *PNAS* 112(43):E5844–53
- Beltran WA, Cideciyan AV, Lewin AS, Iwabe S, Khanna H, et al. 2012. Gene therapy rescues photoreceptor blindness in dogs and paves the way for treating human X-linked retinitis pigmentosa. *PNAS* 109(6):2132–37
- Bennett LD, Metz G, Klein M, Locke KG, Khwaja A, Birch DG. 2019. Regional variations and intra-/intersession repeatability for scotopic sensitivity in normal controls and patients with inherited retinal degenerations. *Investig. Ophthalmol. Vis. Sci.* 60(4):1122–31
- Bermond K, Wobbe C, Tarau IS, Heintzmann R, Hillenkamp J, et al. 2020. Autofluorescent granules of the human retinal pigment epithelium: phenotypes, intracellular distribution, and age-related topography. *Investig. Ophthalmol. Vis. Sci.* 61(5):35
- Berson EL. 1980. Light deprivation and retinitis pigmentosa. *Vis. Res.* 20:1179–84
- Birch DG, Cheng P, Duncan JL, Ayala AR, Maguire MG, et al. 2020. The RUSH2A study: best-corrected visual acuity, full-field electroretinography amplitudes, and full-field stimulus thresholds at baseline. *Transl. Vis. Sci. Technol.* 9(11):9
- Birch DG, Wen Y, Locke K, Hood DC. 2011. Rod sensitivity, cone sensitivity, and photoreceptor layer thickness in retinal degenerative diseases. *Investig. Ophthalmol. Vis. Sci.* 52(10):7141–47
- Bizheva K, Pflug R, Hermann B, Považay B, Sattmann H, et al. 2006. Optophysiology: depth-resolved probing of retinal physiology with functional ultrahigh-resolution optical coherence tomography. *PNAS* 103(13):5066–71
- Boulton M, Dayhaw-Barker P. 2001. The role of the retinal pigment epithelium: topographical variation and ageing changes. *Eye* 15(3):384–89
- Calzetti G, Levy RA, Cideciyan AV, Garafalo AV, Roman AJ, et al. 2018. Efficacy outcome measures for clinical trials of USH2A caused by the common c.2299delG mutation. *Am. J. Ophthalmol.* 193:114–29
- Chang J, Cideciyan AV, Jacobson SG, Sumaroka A, Schwartz SB, et al. 2016. Variegated yet non-random rod and cone photoreceptor disease patterns in RPGR-ORF15-associated retinal degeneration. *Hum. Mol. Genet.* 25(24):5444–59
- Chang J, Jacobson SG, Heon E, Roman AJ, McGuigan DB, et al. 2017. Pupillary light reflexes in severe photoreceptor blindness isolate the melanopic component of intrinsically photosensitive retinal ganglion cells. *Investig. Ophthalmol. Vis. Sci.* 58(7):3215–24
- Cideciyan AV. 2010. Leber congenital amaurosis due to RPE65 mutations and its treatment with gene therapy. *Prog. Retin. Eye Res.* 29(5):398–427
- Cideciyan AV, Aguirre GK, Jacobson SG, Butt OH, Schwartz SB, et al. 2015a. Pseudo-fovea formation after gene therapy for RPE65-LCA. *Investig. Ophthalmol. Vis. Sci.* 56(1):526–37
- Cideciyan AV, Aleman TS, Boye SL, Schwartz SB, Kaushal S, et al. 2008. Human gene therapy for RPE65 isomerase deficiency activates the retinoid cycle of vision but with slow rod kinetics. *PNAS* 105(39):15112–17
- Cideciyan AV, Aleman TS, Jacobson SG, Khanna H, Sumaroka A, et al. 2007a. Centrosomal-ciliary gene CEP290/NPHP6 mutations result in blindness with unexpected sparing of photoreceptors and visual brain: implications for therapy of Leber congenital amaurosis. *Hum. Mutat.* 28(11):1074–83
- Cideciyan AV, Aleman TS, Swider M, Schwartz SB, Steinberg JD, et al. 2004. Mutations in ABCA4 result in accumulation of lipofuscin before slowing of the retinoid cycle: a reappraisal of the human disease sequence. *Hum. Mol. Genet.* 13(5):525–34
- Cideciyan AV, Chang J, Roman AJ, Sheplock R, Garafalo AV, et al. 2018a. Progression in X-linked retinitis pigmentosa due to ORF15-RPGR mutations: assessment of localized vision changes over 2 years. *Investig. Ophthalmol. Vis. Sci.* 59(11):4558–66
- Cideciyan AV, Chang J, Swider M, Sheplock R, McGuigan DB, et al. 2016. Comparative measurements of rod function in retinal degenerations with two-color dark-adapted perimetry. *Investig. Ophthalmol. Vis. Sci.* 57(12):131
- Cideciyan AV, Haeseleer F, Fariss RN, Aleman TS, Jang GF, et al. 2000. Rod and cone visual cycle consequences of a null mutation in the 11-cis-retinol dehydrogenase gene in man. *Vis. Neurosci.* 17(5):667–78



- Cideciyan AV, Hauswirth WW, Aleman TS, Kaushal S, Schwartz SB, et al. 2009a. Vision 1 year after gene therapy for Leber's congenital amaurosis. *N. Engl. J. Med.* 361(7):725–27
- Cideciyan AV, Hood DC, Huang Y, Banin E, Li ZY, et al. 1998. Disease sequence from mutant rhodopsin allele to rod and cone photoreceptor degeneration in man. *PNAS* 95(12):7103–8
- Cideciyan AV, Hufnagel RB, Carroll J, Sumaroka A, Luo X, et al. 2013a. Human cone visual pigment deletions spare sufficient photoreceptors to warrant gene therapy. *Hum. Gene Ther.* 24(12):993–1006
- Cideciyan AV, Jacobson SG. 2019. Leber congenital amaurosis (LCA): potential for improvement of vision. *Investig. Ophthalmol. Vis. Sci.* 60(5):1680–95
- Cideciyan AV, Jacobson SG, Aleman TS, Gu D, Pearce-Kelling SE, et al. 2005a. *In vivo* dynamics of retinal injury and repair in the *rhodopsin* mutant dog model of human retinitis pigmentosa. *PNAS* 102(14):5233–38
- Cideciyan AV, Jacobson SG, Beltran WA, Sumaroka A, Swider M, et al. 2013b. Human retinal gene therapy for Leber congenital amaurosis shows advancing retinal degeneration despite enduring visual improvement. *PNAS* 110(6):E517–25
- Cideciyan AV, Jacobson SG, Drack AV, Ho AC, Charng J, et al. 2019. Effect of an intravitreal antisense oligonucleotide on vision in Leber congenital amaurosis due to a photoreceptor cilium defect. *Nat. Med.* 25(2):225–28
- Cideciyan AV, Jacobson SG, Ho AC, Garafalo AV, Roman AJ, et al. 2021. Durable vision improvement after a single treatment with antisense oligonucleotide seprofarsen: a case report. *Nat. Med.* In press
- Cideciyan AV, Jacobson SG, Roman AJ, Sumaroka A, Wu V, et al. 2020. Rod function deficit in retained photoreceptors of patients with class B Rhodopsin mutations. *Sci. Rep.* 10(1):12552
- Cideciyan AV, Pugh EN, Lamb TD, Huang Y, Jacobson SG. 1997. Rod plateaux during dark adaptation in Sorsby's fundus dystrophy and vitamin A deficiency. *Investig. Ophthalmol. Vis. Sci.* 38(9):1786–94
- Cideciyan AV, Rachel RA, Aleman TS, Swider M, Schwartz SB, et al. 2011. Cone photoreceptors are the main targets for gene therapy of NPHP5 (IQCB1) or NPHP6 (CEP290) blindness: generation of an all-cone Nphp6 hypomorph mouse that mimics the human retinal ciliopathy. *Hum. Mol. Genet.* 20(7):1411–23
- Cideciyan AV, Sudharsan R, Dufour VL, Massengill MT, Iwabe S, et al. 2018b. Mutation-independent rhodopsin gene therapy by knockdown and replacement with a single AAV vector. *PNAS* 115(36):E8547–56
- Cideciyan AV, Swider M, Aleman TS, Roman MI, Sumaroka A, et al. 2007b. Reduced-illumination autofluorescence imaging in ABCA4-associated retinal degenerations. *J. Opt. Soc. Am. A.* 24(5):1457–67
- Cideciyan AV, Swider M, Aleman TS, Sumaroka A, Schwartz SB, et al. 2005b. ABCA4-associated retinal degenerations spare structure and function of the human parapapillary retina. *Investig. Ophthalmol. Vis. Sci.* 46(12):4739–46
- Cideciyan AV, Swider M, Aleman TS, Tsybovsky Y, Schwartz SB, et al. 2009b. ABCA4 disease progression and a proposed strategy for gene therapy. *Hum. Mol. Genet.* 18(5):931–41
- Cideciyan AV, Swider M, Jacobson SG. 2015b. Autofluorescence imaging with near-infrared excitation: normalization by reflectance to reduce signal from choroidal fluorophores. *Investig. Ophthalmol. Vis. Sci.* 56(5):3393–406
- Cideciyan AV, Swider M, Schwartz SB, Stone EM, Jacobson SG. 2015c. Predicting progression of ABCA4-associated retinal degenerations based on longitudinal measurements of the leading disease front. *Investig. Ophthalmol. Vis. Sci.* 56(10):5946–55
- Clarke G, Collins RA, Leavitt BR, Andrews DF, Hayden MR, et al. 2000. A one-hit model of cell death in inherited neuronal degenerations. *Nature* 406(6792):195–99
- Crossland MD, Luong VA, Rubin GS, Fitzke FW. 2011. Retinal specific measurement of dark-adapted visual function: validation of a modified microperimeter. *BMC Ophthalmol.* 11:5
- Delori FC. 1994. Spectrophotometer for noninvasive measurement of intrinsic fluorescence and reflectance of the ocular fundus. *Appl. Opt.* 33(31):7439–52
- Delori FC, Dorey CK, Staurengi G, Arend O, Goger DG, Weiter JJ. 1995. *In vivo* fluorescence of the ocular fundus exhibits retinal pigment epithelium lipofuscin characteristics. *Investig. Ophthalmol. Vis. Sci.* 36(3):718–29
- Drexler W, Morgner U, Ghanta RK, Kärtner FX, Schuman JS, Fujimoto JG. 2001. Ultrahigh-resolution ophthalmic optical coherence tomography. *Nat. Med.* 7(4):502–6



- Ernst W, Faulkner DJ, Hogg CR, Powell DJ, Arden GB, Vaegan. 1983. An automated static perimeter/adaptometer using light emitting diodes. *Br. J. Ophthalmol.* 67(7):431–42
- Feeney L. 1978. Lipofuscin and melanin of human retinal pigment epithelium. Fluorescence, enzyme cytochemical, and ultrastructural studies. *Investig. Ophthalmol. Vis. Sci.* 17(7):583–600
- Gamlin PDR, McDougal DH, Pokorny J, Smith VC, Yau KW, Dacey DM. 2007. Human and macaque pupil responses driven by melanopsin-containing retinal ganglion cells. *Vis. Res.* 47(7):946–54
- Garafalo AV, Cideciyan AV, Héon E, Sheplock R, Pearson A, et al. 2020. Progress in treating inherited retinal diseases: early subretinal gene therapy clinical trials and candidates for future initiatives. *Prog. Retin. Eye Res.* 77:100827
- Gardiner KL, Cideciyan AV, Swider M, Dufour VL, Sumaroka A, et al. 2019. Long-term structural outcomes of late-stage RPE65 gene therapy. *Mol. Ther.* 28(1):266–78
- Gibbs D, Cideciyan AV, Jacobson SG, Williams DS. 2009. Retinal pigment epithelium defects in humans and mice with mutations in MYO7A: imaging melanosome-specific autofluorescence. *Investig. Ophthalmol. Vis. Sci.* 50(9):4386–93
- Gunkel RD. 1967. Retinal profiles: a psychophysical test of rod and cone sensitivity. *Arch. Ophthalmol.* 77(1):22–25
- Guziewicz KE, Cideciyan AV, Beltran WA, Komáromy AM, Dufour VL, et al. 2018. BEST1 gene therapy corrects a diffuse retina-wide microdetachment modulated by light exposure. *PNAS* 115(12):E2839–48
- Haider NB, Jacobson SG, Cideciyan AV, Swiderski R, Streb LM, et al. 2000. Mutation of a nuclear receptor gene, NR2E3, causes enhanced S cone syndrome, a disorder of retinal cell fate. *Nat. Genet.* 24(2):127–31
- Hanany M, Rivolta C, Sharon D. 2020. Worldwide carrier frequency and genetic prevalence of autosomal recessive inherited retinal diseases. *PNAS* 117(5):2710–16
- Hee MR, Bauman CR, Puliafito CA, Duker JS, Reichel E, et al. 1996. Optical coherence tomography of age-related macular degeneration and choroidal neovascularization. *Ophthalmology* 103(8):1260–70
- Hee MR, Puliafito CA, Wong C, Reichel E, Duker JS, et al. 1995. Optical coherence tomography of central serous chorioretinopathy. *Am. J. Ophthalmol.* 120(1):65–74
- Herrera W, Aleman TS, Cideciyan AV, Roman AJ, Banin E, et al. 2008. Retinal disease in Usher syndrome III caused by mutations in the clarin-1 gene. *Investig. Ophthalmol. Vis. Sci.* 49(6):2651–60
- Hood DC, Finkelstein MA. 1986. Sensitivity to light. In *Handbook of Perception and Performance*, Vol. 1, ed. K Boff, L Kaufman, J Thomas, ch. 5. New York: Wiley
- Hood DC, Zhang X, Ramachandran R, Talamini CL, Raza A, et al. 2011. The inner segment/outer segment border seen on optical coherence tomography is less intense in patients with diminished cone function. *Investig. Ophthalmol. Vis. Sci.* 52(13):9703–9
- Huang D, Swanson E, Lin C, Schuman J, Stinson W, et al. 1991. Optical coherence tomography. *Science* 254(5035):1178–81
- Huang Y, Cideciyan AV, Alemán TS, Banin E, Huang J, et al. 2000. Optical coherence tomography (OCT) abnormalities in rhodopsin mutant transgenic swine with retinal degeneration. *Exp. Eye Res.* 70(2):247–51
- Huang Y, Cideciyan AV, Papastergiou GI, Banin E, Semple-Rowland SL, et al. 1998. Relation of optical coherence tomography to microanatomy in normal and rd chickens. *Investig. Ophthalmol. Vis. Sci.* 39(12):2405–16
- Jacobson SG, Aleman TS, Cideciyan AV, Heon E, Golezka M, et al. 2007. Human cone photoreceptor dependence on RPE65 isomerase. *PNAS* 104(38):15123–28
- Jacobson SG, Aleman TS, Cideciyan AV, Roman AJ, Sumaroka A, et al. 2009a. Defining the residual vision in Leber congenital amaurosis caused by RPE65 mutations. *Investig. Ophthalmol. Vis. Sci.* 50(5):2368–75
- Jacobson SG, Aleman TS, Cideciyan AV, Sumaroka A, Schwartz SB, et al. 2005. Identifying photoreceptors in blind eyes caused by RPE65 mutations: prerequisite for human gene therapy success. *PNAS* 102(17):6177–82
- Jacobson SG, Aleman TS, Cideciyan AV, Sumaroka A, Schwartz SB, et al. 2009b. Leber congenital amaurosis caused by Lebercilin (LCA5) mutation: retained photoreceptors adjacent to retinal disorganization. *Mol. Vis.* 15:1098–106
- Jacobson SG, Aleman TS, Sumaroka A, Cideciyan AV, Roman AJ, et al. 2009c. Disease boundaries in the retina of patients with usher syndrome caused by MYO7A gene mutations. *Investig. Ophthalmol. Vis. Sci.* 50(4):1886–94



- Jacobson SG, Borruat FX, Apathy PP. 1990. Patterns of rod and cone dysfunction in Bardet-Biedl syndrome. *Am. J. Ophthalmol.* 109(6):676–88
- Jacobson SG, Cideciyan AV. 2010. Treatment possibilities for retinitis pigmentosa. *N. Engl. J. Med.* 363(17):1669–71
- Jacobson SG, Cideciyan AV, Aleman TS, Sumaroka A, Roman AJ, et al. 2008a. Usher syndromes due to MYO7A, PCDH15, USH2A or GPR98 mutations share retinal disease mechanism. *Hum. Mol. Genet.* 17(15):2405–15
- Jacobson SG, Cideciyan AV, Aleman TS, Sumaroka A, Roman AJ, et al. 2011a. Human retinal disease from AIPL1 gene mutations: foveal cone loss with minimal macular photoreceptors and rod function remaining. *Investig. Ophthalmol. Vis. Sci.* 52(1):70–79
- Jacobson SG, Cideciyan AV, Aleman TS, Sumaroka A, Windsor EAM, et al. 2008b. Photoreceptor layer topography in children with Leber congenital amaurosis caused by RPE65 mutations. *Investig. Ophthalmol. Vis. Sci.* 49(10):4573–77
- Jacobson SG, Cideciyan AV, Gibbs D, Sumaroka A, Roman AJ, et al. 2011b. Retinal disease course in Usher syndrome 1B due to MYO7A mutations. *Investig. Ophthalmol. Vis. Sci.* 52(11):7924–36
- Jacobson SG, Cideciyan AV, Iannaccone A, Weleber RG, Fishman GA, et al. 2000. Disease expression of RP1 mutations causing autosomal dominant retinitis pigmentosa. *Investig. Ophthalmol. Vis. Sci.* 41(7):1898–908
- Jacobson SG, Cideciyan AV, Peshenko IV, Sumaroka A, Olshevskaia EV, et al. 2013a. Determining consequences of retinal membrane guanylyl cyclase (RetGC1) deficiency in human Leber congenital amaurosis en route to therapy: residual cone-photoreceptor vision correlates with biochemical properties of the mutants. *Hum. Mol. Genet.* 22(1):168–83
- Jacobson SG, Cideciyan AV, Ratnakaram R, Heon E, Schwartz SB, et al. 2012. Gene therapy for Leber congenital amaurosis caused by RPE65 mutations: safety and efficacy in 15 children and adults followed up to 3 years. *Arch. Ophthalmol.* 130(1):9–24
- Jacobson SG, Cideciyan AV, Regunath G, Rodriguez FJ, Vandenburgh K, et al. 1995. Night blindness in Sorsby's fundus dystrophy reversed by vitamin A. *Nat. Genet.* 11(1):27–32
- Jacobson SG, Cideciyan AV, Roman AJ, Sumaroka A, Schwartz SB, et al. 2015. Improvement and decline in vision with gene therapy in childhood blindness. *N. Engl. J. Med.* 372(20):1920–26
- Jacobson SG, Cideciyan AV, Sumaroka A, Aleman TS, Schwartz SB, et al. 2006. Remodeling of the human retina in choroideremia: Rab escort protein 1 (REP-1) mutations. *Investig. Ophthalmol. Vis. Sci.* 47(9):4113–20
- Jacobson SG, Cideciyan AV, Sumaroka A, Roman AJ, Charng J, et al. 2017a. Defining outcomes for clinical trials of Leber congenital amaurosis caused by GUCY2D mutations. *Am. J. Ophthalmol.* 177:44–57
- Jacobson SG, Cideciyan AV, Sumaroka A, Roman AJ, Charng J, et al. 2017b. Outcome measures for clinical trials of Leber congenital amaurosis caused by the intronic mutation in the CEP290 gene. *Investig. Ophthalmol. Vis. Sci.* 58(5):2609–22
- Jacobson SG, McGuigan DB, Sumaroka A, Roman AJ, Gruzensky ML, et al. 2016. Complexity of the class B phenotype in autosomal dominant retinitis pigmentosa due to rhodopsin mutations. *Investig. Ophthalmol. Vis. Sci.* 57(11):4847–58
- Jacobson SG, Roman AJ, Aleman TS, Sumaroka A, Herrera W, et al. 2010. Normal central retinal function and structure preserved in retinitis pigmentosa. *Investig. Ophthalmol. Vis. Sci.* 51(2):1079–85
- Jacobson SG, Sumaroka A, Aleman TS, Cideciyan AV, Schwartz SB, et al. 2004. Nuclear receptor NR2E3 gene mutations distort human retinal laminar architecture and cause an unusual degeneration. *Hum. Mol. Genet.* 13(17):1893–902
- Jacobson SG, Sumaroka A, Luo X, Cideciyan AV. 2013b. Retinal optogenetic therapies: clinical criteria for candidacy. *Clin. Genet.* 84(2):175–82
- Jacobson SG, Voigt WJ, Parel JM, Apathy PP, Nghiem-Phu L, et al. 1986. Automated light- and dark-adapted perimetry for evaluating retinitis pigmentosa. *Ophthalmology* 93(12):1604–11
- Johnson CA. 2013. Psychophysical factors that have been applied to clinical perimetry. *Vis. Res.* 90:25–31
- Jonnal RS, Gorczynska I, Migacz JV, Azimipour M, Zawadzki RJ, Werner JS. 2017. The properties of outer retinal band three investigated with adaptive-optics optical coherence tomography. *Investig. Ophthalmol. Vis. Sci.* 58(11):4559–68



- Jonnal RS, Kocaoglu OP, Zawadzki RJ, Lee S-H, Werner JS, Miller DT. 2014. The cellular origins of the outer retinal bands in optical coherence tomography images. *Investig. Ophthalmol. Vis. Sci.* 55(12):7904–18
- Kardon R, Anderson SC, Damarjian TG, Grace EM, Stone E, Kawasaki A. 2011. Chromatic pupillometry in patients with retinitis pigmentosa. *Ophthalmology* 118(2):376–81
- Keilhauer CN, Delori FC. 2006. Near-infrared autofluorescence imaging of the fundus: visualization of ocular melanin. *Investig. Ophthalmol. Vis. Sci.* 47(8):3556–64
- Kitagawa K, Nishida S, Ogura Y. 1989. In vivo quantitation of autofluorescence in human retinal pigment epithelium. *Ophthalmologica* 199(2–3):116–21
- Klein M, Birch DG. 2009. Psychophysical assessment of low visual function in patients with retinal degenerative diseases (RDDs) with the Diagnosys full-field stimulus threshold (D-FST). *Doc. Ophthalmol.* 119(3):217–24
- Kömpf D, Piper HF. 1987. Eye movements and vestibulo-ocular reflex in the blind. *J. Neurol.* 234(5):337–41
- Kowler E. 2011. Eye movements: the past 25 years. *Vis. Res.* 51(13):1457–83
- Krishnan AK, Jacobson SG, Roman AJ, Iyer BS, Garafalo AV, et al. 2020. Transient pupillary light reflex in CEP290- or NPHP5-associated Leber congenital amaurosis: latency as a potential outcome measure of cone function. *Vis. Res.* 168:53–63
- LaVail MM. 1981. Analysis of neurological mutants with inherited retinal degeneration. Friedenwald lecture. *Investig. Ophthalmol. Vis. Sci.* 21(5):638–57
- Leigh RJ, Zee DS. 1980. Eye movements of the blind. *Investig. Ophthalmol. Vis. Sci.* 19(3):328–31
- Lisowska J, Lisowski L, Kelbsch C, Maeda F, Richter P, et al. 2017. Development of a chromatic pupillography protocol for the first gene therapy trial in patients with CNGA3-linked achromatopsia. *Investig. Ophthalmol. Vis. Sci.* 58(2):1274–82
- Litts KM, Zhang Y, Freund KB, Curcio CA. 2018. Optical coherence tomography and histology of age-related macular degeneration support mitochondria as reflectivity sources. *Retina* 38(3):445–61
- Liu Z, Kocaoglu OP, Miller DT. 2016. 3D imaging of retinal pigment epithelial cells in the living human retina. *Investig. Ophthalmol. Vis. Sci.* 57(9):OCT533–43
- Liu Z, Kurokawa K, Hammer DX, Miller DT. 2019. In vivo measurement of organelle motility in human retinal pigment epithelial cells. *Biomed. Opt. Express.* 10(8):4142–58
- Loewenfeld IE, Lowenstein O. 1999. *The Pupil: Anatomy, Physiology, and Clinical Applications*. Boston: Butterworth-Heinemann
- Lowenstein O, Loewenfeld IE. 1959. Influence of retinal adaptation upon the pupillary reflex to light in normal man: part I. Effect of adaptation to bright light on the pupillary threshold. *Am. J. Ophthalmol.* 48(5):536–50
- Lu CD, Lee B, Schottenhamml J, Maier A, Pugh EN, Fujimoto JG. 2017. Photoreceptor layer thickness changes during dark adaptation observed with ultrahigh-resolution optical coherence tomography. *Investig. Ophthalmol. Vis. Sci.* 58(11):4632–43
- Luo X, Cideciyan AV, Iannaccone A, Roman AJ, Ditta LC, et al. 2015. Blue cone monochromacy: visual function and efficacy outcome measures for clinical trials. *PLOS ONE* 10(4):e0125700
- Maguire AM, High KA, Auricchio A, Wright JF, Pierce EA, et al. 2009. Age-dependent effects of RPE65 gene therapy for Leber's congenital amaurosis: a phase 1 dose-escalation trial. *Lancet* 374(9701):1597–605
- Margrain TH, Atkinson D, Binns AM, Fergusson J, Gaffney A, et al. 2020. Functional imaging of the outer retinal complex using high fidelity imaging retinal densitometry. *Sci. Rep.* 10:4494
- Massof RW, Finkelstein D. 1979. Rod sensitivity relative to cone sensitivity in retinitis pigmentosa. *Investig. Ophthalmol. Vis. Sci.* 18(3):263–72
- Matsui R, McGuigan DB, Gruzensky ML, Aleman TS, Schwartz SB, et al. 2016. SPATA7: evolving phenotype from cone-rod dystrophy to retinitis pigmentosa. *Ophthalmic Genet.* 37(3):333–38
- McDougal DH, Gamlin PD. 2010. The influence of intrinsically-photosensitive retinal ganglion cells on the spectral sensitivity and response dynamics of the human pupillary light reflex. *Vis. Res.* 50(1):72–87
- McGuigan DB, Heon E, Cideciyan AV, Ratnapriya R, Lu M, et al. 2017. EYS mutations causing autosomal recessive retinitis pigmentosa: changes of retinal structure and function with disease progression. *Genes* 8(7):178



- McGuigan DB, Roman AJ, Cideciyan AV, Matsui R, Gruzensky ML, et al. 2016. Automated light- and dark-adapted perimetry for evaluating retinitis pigmentosa: filling a need to accommodate multicenter clinical trials. *Investig. Ophthalmol. Vis. Sci.* 57(7):3118–28
- Milam A, Li Z, Fariss R. 1998. Histopathology of the human retina in retinitis pigmentosa. *Prog. Retin. Eye Res.* 17(2):175–205
- Miller D, Kurokawa K. 2020. Cellular scale imaging of transparent retinal structures and processes using adaptive optics optical coherence tomography. *Annu. Rev. Vis. Sci.* 6:115–48
- Paskowitz DM, LaVail MM, Duncan JL. 2006. Light and inherited retinal degeneration. *Br. J. Ophthalmol.* 90(8):1060–66
- Peters S, Kayatz P, Heimann K, Schraermeyer U. 2000. Subretinal injection of rod outer segments leads to an increase in the number of early-stage melanosomes in retinal pigment epithelial cells. *Ophthalmic Res.* 32:52–56
- Pfau M, Lindner M, Müller PL, Birtel J, Finger RP, et al. 2017. Effective dynamic range and retest reliability of dark-adapted two-color fundus-controlled perimetry in patients with macular diseases. *Investig. Ophthalmol. Vis. Sci.* 58:10158–67
- Piccolino FC, Borgia L, Zinicola E, Iester M, Torrielli S, et al. 1996. Pre-injection fluorescence in indocyanine green angiography. *Ophthalmology* 103(11):1837–45
- Poliakov E, Strunnikova NV, Jiang J-k, Martinez B, Parikh T, et al. 2014. Multiple A2E treatments lead to melanization of rod outer segment–challenged ARPE-19 cells. *Mol. Vis.* 20:285–300
- Pollreisz A, Neschi M, Sloan KR, Pircher M, Mittermueller T, et al. 2020. Atlas of human retinal pigment epithelium organelles significant for clinical imaging. *Investig. Ophthalmol. Vis. Sci.* 61(8):13
- Pontikos N, Arno G, Jurkute N, Schiff E, Ba-Abbad R, et al. 2020. Genetic basis of inherited retinal disease in a molecularly characterized cohort of more than 3000 families from the United Kingdom. *Ophthalmology* 127(10):1384–94
- Roman AJ, Cideciyan AV, Aleman TS, Jacobson SG. 2007. Full-field stimulus testing (FST) to quantify visual perception in severely blind candidates for treatment trials. *Physiol. Meas.* 28(8):N51–56
- Roman AJ, Powers CA, Semenov EP, Sheplock R, Aksianiuk V, et al. 2019. Short-wavelength sensitive cone (S-cone) testing as an outcome measure for NR2E3 clinical treatment trials. *Int. J. Mol. Sci.* 20(10):2497
- Roman AJ, Schwartz SB, Aleman TS, Cideciyan AV, Chico JD, et al. 2005. Quantifying rod photoreceptor-mediated vision in retinal degenerations: dark-adapted thresholds as outcome measures. *Exp. Eye Res.* 80(2):259–72
- Roorda A, Duncan JL. 2015. Adaptive optics ophthalmoscopy. *Annu. Rev. Vis. Sci.* 1:19–50
- Sadigh S, Cideciyan AV, Sumaroka A, Huang WC, Luo X, et al. 2013. Abnormal thickening as well as thinning of the photoreceptor layer in intermediate age-related macular degeneration. *Investig. Ophthalmol. Vis. Sci.* 54(3):1603–12
- Sajdak BS, Bell BA, Lewis TR, Luna G, Cornwell GS, et al. 2018. Assessment of outer retinal remodeling in the hibernating 13-lined ground squirrel. *Investig. Ophthalmol. Vis. Sci.* 59(6):2538–47
- Sakami S, Maeda T, Bereta G, Okano K, Golczak M, et al. 2011. Probing mechanisms of photoreceptor degeneration in a new mouse model of the common form of autosomal dominant retinitis pigmentosa due to P23H opsin mutations. *J. Biol. Chem.* 286(12):10551–67
- Scholl HPN, Strauss RW, Singh MS, Dalkara D, Roska B, et al. 2016. Emerging therapies for inherited retinal degeneration. *Sci. Transl. Med.* 8(368):368rv6
- Schraermeyer U, Heimann K. 1999. Current understanding on the role of retinal pigment epithelium and its pigmentation. *Pigment Cell Res.* 12(4):219–36
- Schweitzer NMJ. 1956. Threshold measurements on the light reflex of the pupil in the dark adapted eye. *Doc. Ophthalmol.* 10:1–78
- Simunovic MP, Hess K, Avery N, Mammo Z. 2020. Threshold versus intensity functions in two-colour automated perimetry. *Ophthalmic Physiol. Opt.* 41(1):157–64
- Spaide RF, Curcio CA. 2011. Anatomical correlates to the bands seen in the outer retina by optical coherence tomography: literature review and model. *Retina* 31(8):1609–19
- Sparrow JR, Duncker T, Schuerch K, Paavo M, de Carvalho JRL. 2020. Lessons learned from quantitative fundus autofluorescence. *Prog. Retin. Eye Res.* 74:100774



- Sparrow JR, Gregory-Roberts E, Yamamoto K, Blonska A, Ghosh SK, et al. 2012. The bisretinoids of retinal pigment epithelium. *Prog. Retin. Eye Res.* 31(2):121–35
- Srinivasan VJ, Adler DC, Chen Y, Gorczynska I, Huber R, et al. 2008. Ultrahigh-speed optical coherence tomography for three-dimensional and en face imaging of the retina and optic nerve head. *Investig. Ophthalmol. Vis. Sci.* 49(11):5103–10
- Starengi G, Sadda S, Chakravarthy U, Spaide RF. 2014. Proposed lexicon for anatomic landmarks in normal posterior segment spectral-domain optical coherence tomography: the IN•OCT consensus. *Ophthalmology* 121(8):1572–78
- Stone EM, Andorf JL, Whitmore SS, DeLuca AP, Giacalone JC, et al. 2017. Clinically focused molecular investigation of 1000 consecutive families with inherited retinal disease. *Ophthalmology* 124(9):1314–31
- Strauss RW, Ho A, Muñoz B, Cideciyan AV, Sahel JA, et al. 2016a. The natural history of the progression of atrophy secondary to Stargardt disease (ProgStar) studies: design and baseline characteristics: Progstar Report No. 1. *Ophthalmology* 123(4):817–28
- Strauss RW, Kong X, Bittencourt MG, Ho A, Jha A, et al. 2019. Scotopic microperimetric assessment of rod function in Stargardt disease (SMART) study: design and baseline characteristics (Report No. 1). *Ophthalmic Res.* 61(1):36–43
- Strauss RW, Muñoz B, Jha A, Ho A, Cideciyan AV, et al. 2016b. Comparison of short-wavelength reduced-illumination and conventional autofluorescence imaging in Stargardt macular dystrophy. *Am. J. Ophthalmol.* 168:269–78
- Sumaroka A, Cideciyan AV, Charng J, Wu V, Powers CA, et al. 2019a. Autosomal dominant retinitis pigmentosa due to class B Rhodopsin mutations: an objective outcome for future treatment trials. *Int. J. Mol. Sci.* 20(21):5344
- Sumaroka A, Garafalo AV, Semenov EP, Sheplock R, Krishnan AK, et al. 2019b. Treatment potential for macular cone vision in Leber congenital amaurosis due to CEP290 or NPHP5 mutations: predictions from artificial intelligence. *Investig. Ophthalmol. Vis. Sci.* 60(7):2551–62
- Taubitz T, Fang Y, Biesemeier A, Julien-Schraermeyer S, Schraermeyer U. 2019. Age, lipofuscin and melanin oxidation affect fundus near-infrared autofluorescence. *EBioMedicine* 48:592–604
- Thompson DA, Iannaccone A, Ali RR, Arshavsky VY, Audo I, et al. 2020. Advancing clinical trials for inherited retinal diseases: recommendations from the second Monaciano symposium. *Transl. Vis. Sci. Technol.* 9(7):2
- Tikidji-Hamburyan A, Reinhard K, Storch R, Dietter J, Seitter H, et al. 2017. Rods progressively escape saturation to drive visual responses in daylight conditions. *Nat. Commun.* 8:1813
- von Rückmann A, Fitzke FW, Bird AC. 1995. Distribution of fundus autofluorescence with a scanning laser ophthalmoscope. *Br. J. Ophthalmol.* 79(5):407–12
- Weinberger AWA, Lappas A, Kirschkamp T, Mazinani BAE, Huth JK, et al. 2006. Fundus near infrared fluorescence correlates with fundus near infrared reflectance. *Investig. Ophthalmol. Vis. Sci.* 47(7):3098–108
- Weiter JJ, Delori FC, Wing GL, Fitch KA. 1986. Retinal pigment epithelial lipofuscin and melanin and choroidal melanin in human eyes. *Investig. Ophthalmol. Vis. Sci.* 27(2):145–52
- Weng J, Mata NL, Azarian SM, Tzekov RT, Birch DG, Travis GH. 1999. Insights into the function of rim protein in photoreceptors and etiology of Stargardt's disease from the phenotype in ABCR knockout mice. *Cell* 98(1):13–23
- Wojno AP, Pierce EA, Bennett J. 2013. Seeing the light. *Sci. Transl. Med.* 5(175):175fs8
- Wright AF, Jacobson SG, Cideciyan AV, Roman AJ, Shu X, et al. 2004. Lifespan and mitochondrial control of neurodegeneration. *Nat. Genet.* 36(11):1153–58
- Zawadzki RJ, Jones SM, Olivier SS, Zhao M, Bower BA, et al. 2005. Adaptive-optics optical coherence tomography for high-resolution and high-speed 3D retinal in vivo imaging. *Opt. Express* 13(21):8532–46
- Zeavin BH, Wald G. 1956. Rod and cone vision in retinitis pigmentosa. *Am. J. Ophthalmol.* 42(4):253–69
- Zelinger L, Cideciyan AV, Kohl S, Schwartz SB, Rosenmann A, et al. 2015. Genetics and disease expression in the CNGA3 form of achromatopsia: steps on the path to gene therapy. *Ophthalmology* 122(5):997–1007
- Zhang N, Tsybovsky Y, Kolesnikov AV, Rozanowska M, Swider M, et al. 2015. Protein misfolding and the pathogenesis of ABCA4-associated retinal degenerations. *Hum. Mol. Genet.* 24(11):3220–37
- Zhang T, Kho AM, Yiu G, Srinivasan VJ. 2021. Visible light optical coherence tomography (OCT) quantifies subcellular contributions to outer retinal band 4. *Transl. Vis. Sci. Technol.* 10:30

